Cement and Concrete Research 191 (2025) 107809

Contents lists available at ScienceDirect

Cement and Concrete Research

journal homepage: www.elsevier.com/locate/cemconres

Nonlinear creep of concrete: Stress-activated stick–slip transition of viscous interfaces and microcracking-induced damage

Rodrigo Díaz Flores, Christian Hellmich, Bernhard Pichler *

Institute for Mechanics of Materials and Structures, TU Wien (Vienna University of Technology), Austria

ARTICLE INFO

Keywords:
Nonlinear viscoelasticity
Damage mechanics
Secondary creep
Tertiary creep
Micromechanics
Affinity concept
Sustained loading
Cracking

ABSTRACT

With the aim to identify the mechanisms governing nonlinear basic creep of concrete under uniaxial compression, a micromechanics model is presented. Extending the affinity concept for nonlinear creep, it describes that every microcrack incrementally increases the damage of concrete, leading to a step-wise increase of its compliance. Experimental data are taken from the literature. Strain and acoustic emission measurements from a multi-stage creep test are used to develop the model. This includes identification of microcrack evolution laws for both short-term load application and sustained loading. Strain measurements from four single-stage creep tests are used for model validation. It is concluded that nonlinear creep of concrete is governed by two mechanisms: (i) stress-induced stick–slip transition of viscous interfaces at the nanostructure of cement paste, which is phenomenologically accounted for by the affinity concept, and (ii) microcracking-induced damage, which is of major importance once the stress exceeds some 70% of the strength.

1. Introduction

The prediction of the long-term performance of infrastructure demands material models that accurately describe time-dependent stress–strain relations, including the increase of deformation under constant stress ("creep"), and the inverse process, i.e. the decrease of stress under constant deformation ("relaxation"). Relaxation of concrete beneficially reduces stresses in tunnel linings, both on the short term, e.g. in young shotcrete tunnel shells [1,2], and on the long term, e.g. in precast reinforced concrete segments called tubbings [3]. Creep of concrete results in ever increasing deflections of bridges, putting their serviceability at stake [4,5], and it reduces prestress in prestressed concrete structures, e.g. in nuclear containment buildings, resulting in an increased risk of leakage [6–8]. Concrete creeps *linearly* at low degrees of utilization, i.e. stress-to-strength ratios, σ/σ_{ult}, smaller than some 40%, implying that the delayed strains scale *linearly* with the imposed stress. Concrete creeps *nonlinearly* in the regime $\sigma/\sigma_{ult} \gtrapprox 40\%$, implying that the delayed strains scale *overlinearly* with the imposed stress [9,10].

As regards modeling of nonlinear creep, several models exist. The microprestress-solidification theory [11,12] has been used for modeling aging nonlinear creep of concrete subjected to uniaxial compression at different stress-to-strength ratios [13], as well as to simulate the coupling between drying, microcracking, and creep [14]. These couplings have also been investigated using a poromechanical formulation, under the additional consideration of stress and strain multiaxiality and temperature variations [15]. Such advanced models typically require the optimization of several parameters in order to accurately reproduce specific experimental data. The affinity concept represents a simple, yet effective way of accounting for nonlinear creep [10]. It is based on the observation that creep strain histories resulting from constant stresses remain qualitatively similar even in the nonlinear range, such that nonlinear creep is "affine" to linear creep. In mathematical terms, this reads as [10]

$$\varepsilon(t, \sigma/\sigma_{ult}) = \varepsilon_0(\sigma/\sigma_{ult}) + \varphi_{lin}(t)\,\eta(\sigma/\sigma_{ult})\,\varepsilon_0(\sigma/\sigma_{ult}), \tag{1}$$

where $\varepsilon_0(\sigma/\sigma_{ult})$ refers to the strain resulting from quasi-instantaneous load application, $\varphi_{lin}(t)$ denotes a time-dependent coefficient describing linear creep, and η is an amplification factor for nonlinear creep. It was introduced as [10]

$$\eta = 1 + 2\left[\frac{\sigma}{\sigma_{ult}}\right]^4. \tag{2}$$

Notably, potential damage of concrete resulting from quasi-instantaneous load application is implicitly accounted for in $\varepsilon_0(\sigma/\sigma_{ult})$. Thus, the affinity concept takes into account both (i) potential microcracking under quasi-instantaneous load application, see the first appearance of $\varepsilon_0(\sigma/\sigma_{ult})$ in Eq. (1), and (ii) the resulting amplification of creep of concrete, see $\varepsilon_0(\sigma/\sigma_{ult})$ multiplied by $\varphi_{lin}(t)$ in Eq. (1). The

* Corresponding author.
E-mail address: bernhard.pichler@tuwien.ac.at (B. Pichler).

https://doi.org/10.1016/j.cemconres.2025.107809
Received 13 August 2024; Received in revised form 20 December 2024; Accepted 26 January 2025
Available online 16 February 2025

affinity concept has been shown to be applicable for secondary creep, in the regime $\sigma/\sigma_{ult} \lessapprox 70\%$ [10].

The mechanisms representing the microstructural origin of nonlinear creep of concrete are still to be clarified. It is often agreed that damage induced by microcracking plays an important role in nonlinear creep [13,16,17], as indicated through correlations between delayed strains and acoustic emissions [18,19]. This role was further corroborated through quantification of microcracking at failure under sustained loading, which has evidenced a state of much larger damage than the one observed at failure under quasi-static monotonous load increase [20,21]. Damage induced by cracking is considered to be responsible for tertiary creep of concrete, which leads to failure under sustained loading which is smaller than the strength of the material [22–24]. However, other researchers have found that nonlinear creep does not yield a significant degradation of concrete [25–28]. These contributions point toward nonlinear viscoelastic phenomena which are independent of microcracking [29].

In this study, an analytical model for nonlinear creep of concrete under uniaxial compression will be developed. It is focused on nonaging basic creep of concrete exposed to isothermal conditions, where the influences of aging [30,31], drying [11,32–34], and temperature changes [35,36] are negligible. The model includes consideration of two mechanisms: (i) nonlinear viscoelastic phenomena and (ii) microcracking-induced damage of concrete during quasi-instantaneous load application *and* sustained loading. As for contribution (i), the affinity parameter η for nonlinear creep will be interpreted by means of micromechanics models [37–40] explaining that macroscopic creep results from viscous gliding of nanoscopic interfaces lubricated by confined water. As for contribution (ii), experimental results from a multi-stage nonlinear creep test [18], monitored with the acoustic emissions technique, will be used for the development of a damage model describing that every microcrack, no matter whether it is created during short-term load application or sustained loading, increases the damage of concrete by always the same incremental value, leading to a proportional increase of the compliance (= the inverse of the stiffness) of concrete. Evolution laws for the creation of microcracks during quasi-instantaneous and sustained loading will be identified, finally allowing for the simulation of creep tests in which acoustic emissions have not been measured.

The paper is structured as follows. Section 2 refers to the experimental results of the multi-stage nonlinear creep test of Rossi et al. [18]. Section 3 is focused on the proposed micromechanics-informed model for nonlinear creep of concrete, including the micromechanical interpretation of the affinity parameter η. Section 4 deals with the evolution laws for the creation of microcracks. Section 5 presents model predictions and simulations of other nonlinear creep tests. Section 6 contains the discussion of the obtained results. Section 7 closes the paper with conclusions drawn from the results of the presented study.

2. Rossi et al.'s [18] multilevel uniaxial compression creep testing of concrete at stress-to-strength ratios larger than 50%

2.1. Experimental data

The first three load stages of the multilevel test by Rossi et al. [18] can be analyzed in detail, as the data provided in [18] allow for identifying the evolution of both the strains *and* the acoustic events as functions of *time*. As regards the fourth and the fifth load stage, the acoustic events are only available as a function of the strains. These data will be used in Section 4.

Rossi et al. [18,41] produced concrete cylinders with diameters of 16 cm and heights of 100 cm from ordinary Portland cement (OPC), water, and limestone aggregates, see Table 1 for composition details. The specimens were protected against drying both before and during testing [18,41].

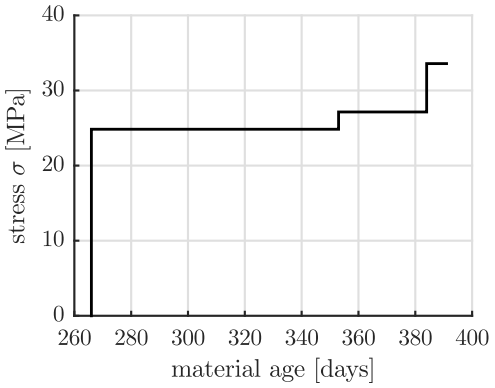

Fig. 1. History of uniaxial compressive stress imposed by Rossi et al. [18] on concrete cylinders during the first three stages of the multilevel creep test, see also Table 2.

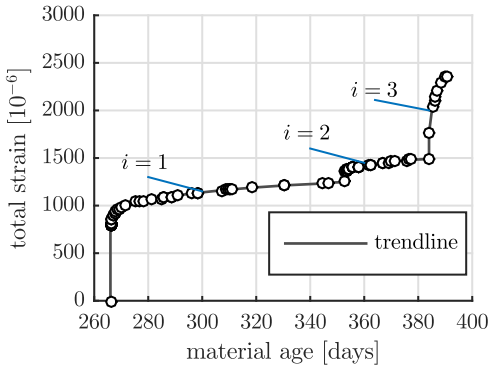

Fig. 2. History of normal compressive strains measured by Rossi et al. [18] on concrete cylinders subjected to the history of uniaxial compressive stresses illustrated in Fig. 1.

The multilevel creep experiment of [18] was started 266 days after material production and lasted for 125 days, see Fig. 1 and Table 2 for the first three load stages. During creep testing, the axial normal strain was measured, see Fig. 2. These strains are by more than three orders of magnitude larger than the autogenous shrinkage strains [18]. Accordingly, the uniaxial compression tests delivered *basic* creep properties, as aging and drying effects were comparatively negligible. In addition, the evolution of acoustic events occurring inside the specimen were recorded, see Fig. 3.

The stress-to-strength ratios reported in [18] are equal to the stresses imposed on the *266 days* old concrete *cylinders*, divided by the *cube* compressive strength determined *28 days* after production:

$$\sigma_{ult,cube,28d} = 46\,\text{MPa}\,. \tag{3}$$

Herein, actual stress-to-strength ratios will be used. The strength at the start of the multilevel creep test, i.e. at the age of 266 days, is estimated based on Eq. (3), the strength evolution of a nominally identical concrete [41], as well as Table 5.1-3 and Eq. (5.1-50) of the fib Model Code of [42], see Appendix B.1. This yields three different values: $\sigma_{ult,1} = 43.0\,\text{MPa}$, $\sigma_{ult,2} = 44.5\,\text{MPa}$, and $\sigma_{ult,3} = 46.0\,\text{MPa}$. This moderate uncertainty regarding the strength propagates through the following analysis. Uncertainty propagation is as made visible through the use of index $k = 1, 2, 3$, see e.g. Table 3.

The hydration degrees associated with the three strength values are identified by means of the validated multiscale strength model described in [43]. The three identified values of the hydration degree, $\xi \approx \{84\%\ ;\ 86\%\ ;\ 88\%\}$, see also Table 3, together with the specific initial composition of the analyzed concrete, see Table 1, allow for predicting the elastic modulus and the creep modulus by means of the validated multiscale creep model described in [44]. The moduli

Table 1
Initial composition of the concrete cylinders, with volume $V = 0.020106\,\mathrm{m}^3$, tested by Rossi et al. [18,41]: the listed data imply an initial water-to-cement mass ratio $w/c = 0.54$, a volume fraction of cement paste $f_{cp} = 0.292$, and a volume fraction of aggregates, $f_{agg} = 0.708$.

Component [18]	Dosage [18]	Mass Density	Volume fraction
Cement: CEM I 52.5 N	$340.00\,\mathrm{kg/m^3}$	$3150\,\mathrm{kg/m^3}$	0.108
Water	$184.22\,\mathrm{kg/m^3}$	$1000\,\mathrm{kg/m^3}$	0.184
Dried sand-lime aggregate 0/4	$739.45\,\mathrm{kg/m^3}$	$2560\,\mathrm{kg/m^3}$	0.289
Dried sand-lime aggregate 6.3/20	$1072.14\,\mathrm{kg/m^3}$	$2560\,\mathrm{kg/m^3}$	0.419
Sum:	$2335.81\,\mathrm{kg/m^3}$		1.000

Table 2
Stresses imposed during the first three stages of multilevel creep testing, after [18], see also Fig. 1.

Stage	"Stress-to-strength ratio" [41]	Duration of stage [41]	Stress	Time of application
$i = 1$	$\sigma/\sigma_{ult,cube,28d} = 54\%$	87 days	$\sigma_1 = 24.9\,\mathrm{MPa}$	$t_1 = 266.00\,\mathrm{days}$
$i = 2$	$\sigma/\sigma_{ult,cube,28d} = 59\%$	31 days	$\sigma_2 = 27.3\,\mathrm{MPa}$	$t_2 = 353.00\,\mathrm{days}$
$i = 3$	$\sigma/\sigma_{ult,cube,28d} = 73\%$	7 days	$\sigma_3 = 33.6\,\mathrm{MPa}$	$t_3 = 384.00\,\mathrm{days}$

Table 3
Mechanical properties of the 266 day old OPC concrete tested by Rossi et al. [18]; the initial water-to-cement mass ratio $w/c = 0.54$, the reference time $\tau_{ref} = 1\,\mathrm{day}$, the creep exponent $\beta = 0.25$, and the internal relative humidity $RH = 0.95$ apply to all three estimates of the 266 day strength; $k = 1, 2, 3$ refers to the uncertainty regarding the strength of the tested concrete, see also Appendix B.1.

estimate of 266 day strength $\sigma_{ult,k}$ [MPa]	index k [–]	hydration degree ξ_k [–]	elastic modulus E_k [GPa]	creep modulus $E_{c,k}$ [GPa]
lower estimate = 43.0	1	0.84	30.9	190.2
medium estimate = 44.5	2	0.86	31.2	195.4
higher estimate = 46.0	3	0.88	31.6	200.7

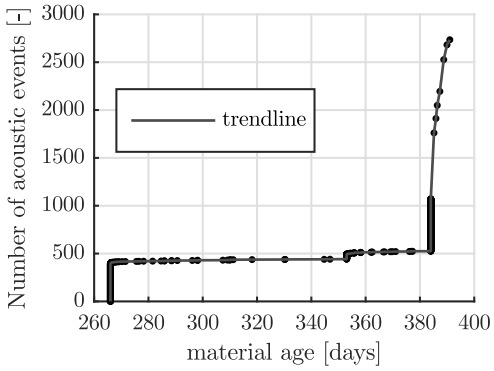

Fig. 3. Number of acoustic events measured by Rossi et al. [18] during the first three load stages of the multilevel creep test.

range from 30.9 GPa to 31.6 GPa and from 190.2 GPa to 200.7 GPa, respectively, see Table 3. The internal relative humidity is estimated from experimental data provided by humidity-sensitive capacitive sensors cast into epoxy resin-sealed samples with $w/c = 0.54$, which were cured at 20 °C for 300 days [45], proposing $RH = 0.95$. This value is confirmed by samples stored in cylindrical test tubes throughout one year [46].

2.2. Interpretation of the acoustic measurements by Rossi et al. [18]

Rossi et al. [18] mounted two pairs of acoustic sensors to their 100 cm-long concrete cylinders: at distances of 8 cm and 18 cm, respectively, from each of the two loaded surfaces, see [18, Fig. 1]. This arrangement allowed for detecting and excluding signals coming from the load application system. Signals coming from the sample were amplified and filtered. They were recorded provided that the peak amplitude exceeded 250 mV. The frequency spectrum curve of every acoustic event was integrated over the low frequency (LF) band $[\,0\,;125\,]$ Hz, the medium frequency (MF) band $[\,125\,;250\,]$ Hz, and the high frequency (HF) band $[\,250\,;375\,]$ Hz. Corresponding energy fractions were calculated by dividing each of the three integrals by the total area under the frequency spectrum curve. These energy fractions are referred to as φ_{LF}, φ_{MF}, and φ_{HF}. Every acoustic event was classified according to the low-to-medium energy fraction ratio: Group 1: $0 \le \varphi_{LF}/\varphi_{MF} < 0.2$, Group 2: $0.2 \le \varphi_{LF}/\varphi_{MF} < 0.5$, Group 3: $0.5 \le \varphi_{LF}/\varphi_{MF} \le 1.0$. During the first load application step, some 10% of the acoustic events fell into Group 1, some 20% fell into Group 2, and some 70% fell into Group 3, see [18, Fig. 9]. This distribution ("signature") of the acoustic events remained the same throughout the remainder of the test, including phases of sustained loading and phases of further load increase [18]. Finding characteristic frequency distributions of the acoustic signals, which remain the same throughout testing, and which are very similar when testing *different* concretes has led to the conclusion that the acoustic events recorded during basic creep testing under uniaxial compression are related to the creation of microcracks [47].

Classification of oscillating waveforms of acoustic events is nowadays typically based on the "average frequency" and the "RA value" [48]. Each time the signal amplitude of one event crosses the threshold level, it is counted as a ringdown, and the "average frequency" of the event is equal to the total number of ringdown counts divided by the time span from the first to the last ringdown. The "RA value" is equal to the maximum amplitude of the signal divided by the rise time which is the time span from the first ringdown to the global maximum of the signal. Tensile cracks create acoustic signals which have significantly larger average frequencies and significantly smaller RA values than the acoustic signals created by shear cracks [48, Fig. 2].[1] Applying the described approach of waveform analysis to acoustic signals recorded in uniaxial compressive strength tests on concrete cylinders with height-to-diameter ratio of 2:1 allowed for demonstrating that tensile mode I cracking dominates both in the pre-peak regime and around the peak load [49, Figs. 11 and 12a]. As regards the spatial origins of microcracking, X-ray Computed Tomography monitoring of uniaxial compression tests on concrete cylinders [50] revealed that mode I microcracking initially occurs disorderly throughout the specimen, which is also referred to as diffuse microcracking [51]. Near the peak load, mode I microcracking localizes into a banded region inclined to the loading axis, with microcracks continuing to run mainly in the axial direction [50].

[1] The described type of waveform analysis is out of reach herein, because the signals recorded by Rossi et al. [18] were not published.

2.3. Implications for the continuum damage modeling approach and its underlying assumptions

Although every single acoustic event is unique, Rossi et al. [18] found that the *population* of all recorded acoustic events had a characteristic "signature" which remained *on average* almost the same throughout the entire test, even though the population of acoustic signals grew progressively. Herein, it is assumed that this invariant statistical "signature" is a feature of *diffuse* microcrack nucleation, as observed by Desrues et al. [50]. In addition it is envisioned that microcrack nucleation at a microstructural position where the local stress reaches the local strength relaxes the former local stress peak. Therefore, it is unlikely that the nucleated microcrack continues to propagate or that an additional microcrack nucleates in the immediate vicinity. Instead, the microcracks are assumed to nucleate disorderly, such that the tested specimen may be treated as *one* representative volume element (RVE). The progressive deterioration of the RVE is described by means of a continuum damage formulation in which every recorded acoustic event is taken as an occasion to increase the damage variable by always the same amount. The corresponding constant crack size a, which will be introduced in the model, is to be interpreted as an *average* crack size which is representative of the actual microcrack population.

3. Micromechanics-inspired approach to nonlinear creep of concrete

3.1. Hereditary mechanics: the linear theory of viscoelasticity

In the linear theory of viscoelasticity, stress and strain histories are related to each other by means of a convolution integral formulation, referred to as Boltzmann's superposition principle [52,53]:

$$\boldsymbol{\varepsilon}(t) = \int_{-\infty}^{t} \mathbb{J}(t-\tau) : \frac{\mathrm{d}\boldsymbol{\sigma}}{\mathrm{d}\tau}\, \mathrm{d}\tau\,, \tag{4}$$

where $\boldsymbol{\varepsilon}$ denotes the linearized strain tensor, $\mathbb{J}$ denotes the creep compliance tensor, $\boldsymbol{\sigma}$ denotes the Cauchy stress tensor, t denotes the recording time during the creep test, τ denotes (past) time instants of loading events triggering delayed effects, and ":" denotes the double-contracting tensor product. Eq. (4) is *linear* in the sense that, if any specific stress history $\boldsymbol{\sigma}(\tau)$ produces a corresponding strain history $\boldsymbol{\varepsilon}(t)$, then a qualitatively identical but amplified stress history, $\alpha \times \boldsymbol{\sigma}(\tau)$, with scalar magnification factor $\alpha > 1$, yields a qualitatively identical strain history which is amplified by the same magnification factor: $\alpha \times \boldsymbol{\varepsilon}(t)$.

As for the analysis of creep tests on concrete cylinders subjected to compression in their axial direction, a cylindrical r, φ, z-coordinate system is introduced. The uniaxial compressive stress state history can be expressed as:

$$\boldsymbol{\sigma}(\tau) = \sigma(\tau)\, \mathbf{e}_z \otimes \mathbf{e}_z\,, \tag{5}$$

where $\sigma \geq 0$ is the compressive axial normal stress component prescribed during the experiment, $\mathbf{e}_z$ denotes the unit base vector in axial direction, and $\otimes$ stands for the dyadic vector product.[2] Since concrete is isotropic, the resulting strain history reads as

$$\boldsymbol{\varepsilon}(t) = \varepsilon(t)\, \mathbf{e}_z \otimes \mathbf{e}_z + \varepsilon_{lat}(t) \Big[\mathbf{e}_r \otimes \mathbf{e}_r + \mathbf{e}_\varphi \otimes \mathbf{e}_\varphi \Big]\,, \tag{6}$$

where $\varepsilon \geq 0$ denotes the axial normal strain component describing a shortening of the tested specimen in the direction of loading, $\varepsilon_{lat} \leq 0$ denotes the lateral normal strain component describing a widening of the tested specimen in directions orthogonal to the axis of loading. $\mathbf{e}_r$ and $\mathbf{e}_\varphi$ denote the unit base vectors in the radial direction and the circumferential direction, respectively. Herein, the focus rests on the axial normal strain. The lateral normal strain is beyond the scope of the present contribution.

The scalar relation between axial stress and strain is extracted from Eq. (4) specialized for Eqs. (5) and (6):

$$\varepsilon_{mod}(t) = \int_{-\infty}^{t} J(t-\tau)\, \frac{\mathrm{d}\sigma}{\mathrm{d}\tau}\, \mathrm{d}\tau\,, \tag{7}$$

where J is the uniaxial creep compliance function, with $J(t < \tau) = 0$. The stepwise loading history $\sigma(\tau)$ prescribed by Rossi et al. [18] reads as:

$$\sigma(\tau) = \sum_{i=1}^{n} \big[\sigma_i - \sigma_{i-1}\big]\, H(\tau - t_i)\,, \tag{8}$$

where n denotes the number of stress steps, σ_i is the stress imposed at time instant t_i, with $\sigma_0 = 0$, and $H(t - t_i)$ denotes the Heaviside step function which is equal to 0 for $t < t_i$ and equal to 1 for $t > t_i$. Inserting Eq. (8) into Eq. (7), noting that the derivative of the Heaviside step function is the Dirac function $\delta(t)$ which is infinite at $t = 0$ and zero elsewhere, while the integral over the singularity yields again the Heaviside function, eventually yields

$$\varepsilon_{mod}(t) = \sum_{i=1}^{n} J(t - t_i) \big[\sigma_i - \sigma_{i-1}\big]\, H(t - t_i)\,. \tag{9}$$

The remainder of this section is aimed at deriving a simple yet realistic mathematical format of the creep compliance function $J(t - t_i)$. For this purpose, the microstructural sources of instantaneous elastic versus delayed creep deformations are well distinguished.

3.2. Crack micromechanics-informed linear viscoelasticity

For the viscoelastic response of linear creeping concrete, we consider the microstress fields around microcracks evolving in a matrix of undamaged concrete, as depicted in the leftmost RVE of Fig. 4(a). These fields can be modeled in the framework of continuum micro(poro)mechanics [54,55], in association with a two-phase composite consisting of an undamaged concrete matrix with linear viscoelastic compliance tensor $\mathbb{J}(t - \tau)$, hosting interacting (yet not intersecting) penny-shaped microcracks [56]. Homogenizing the stiffness of the described composite by means of (i) transforming the time-dependent problem into the Laplace-Carson space, (ii) using the Mori–Tanaka scheme [57,58] for a series of quasi-elastic stiffness upscaling problems, and (iii) back-transformation into the time domain, yields [59,60]

$$\mathbb{J}_{dam}(t-\tau) = \left[\mathbb{I} + \frac{4\pi}{3}\, \omega\, \mathbb{T}\right] : \mathbb{J}(t-\tau)\,, \tag{10}$$

where $\mathbb{J}_{dam}(t - \tau)$ denotes the linear viscoelastic compliance tensor of damaged concrete, $\mathbb{I}$ denotes the symmetric fourth-order identity tensor, and $\omega \geq 0$ is Budiansky and O'Connell's scalar and dimensionless microcrack density parameter [61]. As for penny-shaped microcracks characterized by a radius a, the microcrack density parameter reads as:

$$\omega = \frac{N\, a^3}{V}\,, \tag{11}$$

where N is the number of microcracks inside a representative volume V of damaged concrete. $\mathbb{T}$ in Eq. (10) stands for a tensor which accounts for orientational properties of the microcrack network. Being a function of Poisson's ratio ν of undamaged concrete, analytical expressions for $\mathbb{T}$ are available in the literature [56,59]. Eq. (10) underscores that the effective viscoelastic compliance of damaged concrete increases linearly with increasing damage variable ω. As ω approaches infinity, the viscoelastic compliance approaches infinity, i.e. the viscoelastic stiffness approaches zero.

[2] A positive mathematical sign is used for compression and contraction, while a negative sign refers to tension and expansion.

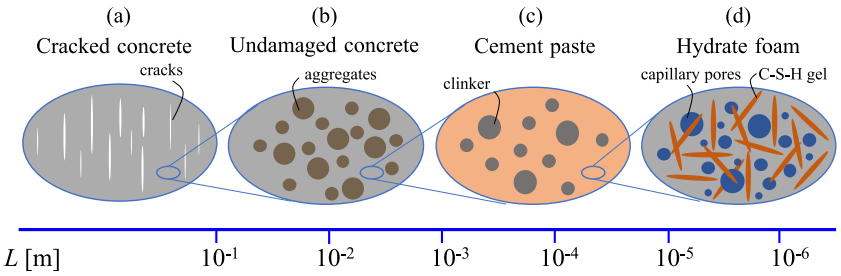

Fig. 4. Continuum micromechanics organogram showing qualitative properties of the hierarchically organized structure of concrete; two-dimensional sketches refer to three-dimensional representative volume elements of (a) damaged concrete, (b) undamaged concrete, (c) cement paste, and (d) hydrate foam.

A one-dimensional isotropic version of Eq. (10) can be given in terms of the scalar linear viscoelastic compliance functions of damaged and undamaged concrete, $J_{dam}(t-\tau)$ and $J(t-\tau)$, respectively [56,62]

$$J_{dam}(t-\tau) = \left[1 + \frac{N}{V}\, a^3 f(\nu)\right] J(t-\tau)\,. \tag{12}$$

The function $f(\nu)$ depends on orientational properties of the microcrack network. It is analytically known only for isotropically oriented and for parallel microcracks [56,62]. However, microcracks developing in concrete under uniaxial compression will neither be isotropically oriented nor parallel. Therefore, $f(\nu)$ is unknown in the present case. The characteristic size of the microcracks, a, is also unknown. This provides the motivation to introduce a damage factor γ as

$$\gamma^3 = a^3\, f(\nu)\,. \tag{13}$$

If this model approach is realistic, then one constant value of γ would be able to represent the entirety of the multilevel creep test of Rossi et al. [18], as depicted in Figs. 1 and 2.

3.3. Damage-dependent nonlinear creep evolving in viscous interfaces pervading the C-S-H gel

The nonlinear viscoelastic response of damaged concrete is described by a creep function reading as

$$J_{dam}(t-t_i) = \left[1 + \frac{\gamma^3\, N(t)}{V}\right] \left\{ \frac{1}{E} + \frac{\eta_i\, RH}{E_c} \left[\frac{t-t_i}{t_{ref}}\right]^{\beta} \right\}. \tag{14}$$

The first term inside the braces of Eq. (14) relates to the instantaneous elastic portion, while the following term relates to the delayed material response. The latter is quantified through (i) the creep modulus E_c and the power-law exponent[3] β quantified from the micromechanics model of [44,63], depicted by the three RVEs of Figs. 4(b-d), with the input values taken from Table 3; through (ii) the relative humidity RH (being larger than 40%) functioning as a reduction factor [33,64–68], see Fig. 5; and through (iii) the so-called affinity parameter η_i [10] considering microstructural changes deep inside the undamaged concrete matrix, namely in the C-S-H gel phase of the RVE of Fig. 4(d). The dimensionless affinity parameter is a fourth-order power-law function of the (macroscopic) stress-to-strength ratio [10]:

$$\eta_i = 1 + 2\left[\frac{\sigma_i}{\sigma_{ult}}\right]^4, \tag{15}$$

whereby the imposed stress σ_i refers to the time interval from t_i to t_{i+1}. The affinity parameter introduced in Eq. (15) results in a nonlinearity that goes beyond the limit of applicability of the linear theory of viscoelasticity and the associated superposition principle named after Boltzmann, see Eqs. (4), (7), and (9). Still, the creep function works well for single-stage creep tests such as described by setting n in Eq. (9) equal to 1. As for multilevel nonlinear creep tests, Tasevski et al. [24] proposed an extension of the superposition approach toward the affinity concept. Complementing this approach by the consideration of partial saturation as well as of microcracking-induced damage eventually yields

$$\varepsilon_{mod}(t) = \left[1 + \gamma^3\, \frac{N(t)}{V}\right] \left\{ \frac{\sigma(t)}{E} + \sum_{i=1}^{n} \left[\sigma_i\, \eta_i - \sigma_{i-1}\, \eta_{i-1}\right] \frac{RH}{E_c} \left[\frac{t-t_i}{t_{ref}}\right]^{\beta} H(t-t_i) \right\}. \tag{16}$$

A micromechanical interpretation of this approach will be provided after checking whether Eq. (16) can describe the creep behavior illustrated in Fig. 2, while accounting for the development of microcracks as illustrated in Fig. 3.

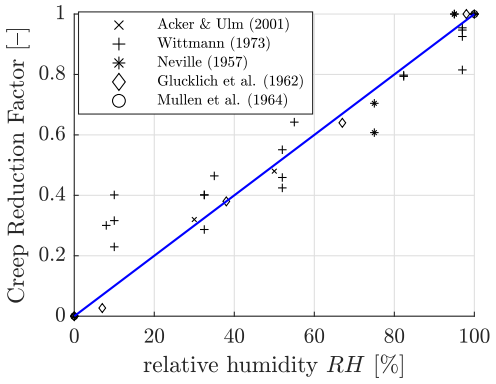

Fig. 5. Creep reduction factor as a function of the internal relative humidity of concrete; experimental data were taken from [33,64,65,67,68].

3.4. Simulation of the multistage basic creep test of Rossi et al. [18] - identification of the damage factor γ

The damage factor γ is unknown. It will be identified such that strains modeled according to Eq. (16) best reproduce the measured strains of Fig. 2. One value of γ will be identified for each one of the sets of material properties listed in Table 3. The identification task is formulated as an optimization problem:

$$\mathcal{E}(\gamma_k) = \sqrt{\frac{1}{m}\sum_{j=1}^{m}\left[\varepsilon_{mod}(\gamma_k; t_j) - \varepsilon_{exp}(t_j)\right]^2} \to \min \qquad \forall k = 1,2,3\,, \tag{17}$$

where $m = 86$ refers to the 86 measured creep strain values illustrated in Fig. 2. The first 78 of these values refer to the time instants at which a new acoustic event was recorded during the first two load plateaus, see Figs. A.14(a)–A.14(b), and the final values points refer to the third load plateau, see Fig. A.14(c).

Other than γ, all input quantities required for evaluation of $\varepsilon_{mod}(t)$ according to Eq. (16) are known. The evolution of the number of

[3] It can be shown that the consideration of a logarithmic creep law after a transition time of 32 days does not significantly improve the model prediction accuracy.

Table 4
Values of the damage factor γ identified for three different sets of the 266 day mechanical properties of the concrete tested by Rossi et al. [18], see also Table 3; $k = 1,2,3$ refers to the uncertainty regarding the strength of the tested concrete, see also Appendix B.1.

index k [–]	damage factor γ_k [mm]	root mean squared error $\mathcal{E}(\gamma_k)$ [10^{-6}]
1	11.7	70.7
2	12.7	59.4
3	13.6	51.8

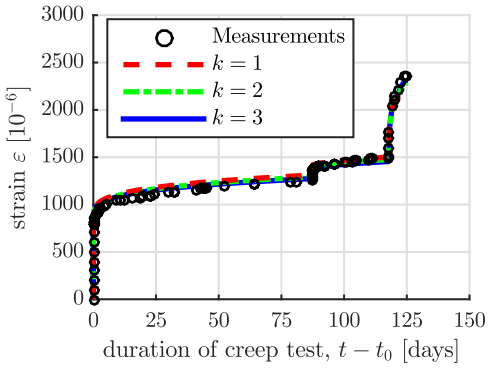

Fig. 6. Comparison of compressive strains computed according to Eq. (16) with the measured strains of Fig. 2; $k = 1,2,3$ refers to the uncertainty regarding the strength of the tested concrete.

microcracks, $N(t)$, is taken from Fig. 3. The volume of the specimen, V, is given in Table 1. The stress history $\sigma(t)$ is given in Eq. (8). The stress values σ_i and σ_{i-1} with $i = 1,2,3$ and corresponding time instants of stress application, t_i, are given in Table 2. The corresponding values of the affinity parameter, η_i and η_{i-1} follow from inserting the values of σ_i from Table 2 together with strength values σ_{ult} from Table 3 into Eq. (2). Note that $\sigma_0 = 0\,\text{MPa}$ and $\eta_0 = 0$. The elastic modulus E, the internal relative humidity RH, the creep modulus E_c, the reference time t_{ref}, and the creep exponent β are listed in Table 3.

Minimizing the root mean squared error between modeled and measured strains three times, i.e. under consideration of three different sets of the 266 day mechanical properties of the tested concrete, see Table 3, allows for identification of three values of the damage factor, see Table 4.

In all three cases, the attainable minimum of the root mean squared errors according to Eq. (17) are quite similar: they range from 51.8×10^{-6} to 70.7×10^{-6}, see Table 4. Thus, the strains modeled based on the maturity-dependent input values of Tables 3 and 4 reproduce the measured strains very well, see Fig. 6.

Fig. 6 underscores that Eq. (16) can indeed describe the creep behavior illustrated in Fig. 2 based a stress-independent value of the damage factor γ, while accounting for the development of microcracks as illustrated in Fig. 3. The following micromechanical interpretation of the affinity parameter η is organized in two steps. In step 1, a rheological model consisting of Kelvin–Voigt units is discussed. Step 2 refers to the transition to matrix-interface composites.

3.5. Nonlinear creep superposition of Eq. (16): Kelvin–Voigt units with stress-dependent spring stiffness and dashpot viscosity

Any creep function can be approximated by means of a Prony series:

$$J(t-\tau) \approx \frac{1}{E_s} + \sum_{k=1}^{m} \frac{1}{E_k}\left[1 - \exp\left(-\frac{E_k\,[t-\tau]}{\mu_k}\right)\right]. \tag{18}$$

The corresponding rheological model consists of one elastic spring with stiffness $E_s = E/\left(1+\gamma^3\,N(t)/V\right)$ being serially arranged with m Kelvin–Voigt units, i.e. with parallel arrangements of one spring and one dashpot each, see Fig. 7. As for the kth Kelvin–Voigt unit, the stiffness of the spring is denoted as E_k and the viscosity of the dashpot as μ_k. Because of the serial arrangement, all Kelvin–Voigt units experience the same stress. Therefore, we may focus on the kth Kelvin–Voigt unit. Its creep function reads as:

$$J(t-\tau) = \frac{1}{E_k}\left[1 - \exp\left(-\frac{E_k\,[t-\tau]}{\mu_k}\right)\right]. \tag{19}$$

The stress experienced by the Kelvin–Voigt unit, $\sigma(t)$, is the sum of the stress prevailing in the spring, $\sigma_{spring}(t) = E_k\,\varepsilon(t)$, and the one prevailing in the dashpot, $\sigma_{dashpot}(t) = \mu_k\,\dot{\varepsilon}(t)$, where $\dot{\varepsilon}$ stands for the time-derivative of ε. Thus, the stress–strain behavior described by the kth Kelvin–Voigt unit can be expressed as [39]

$$\dot{\varepsilon}(t) + \varepsilon(t)\,\frac{E_k}{\mu_k} = \frac{\sigma(t)}{\mu_k}. \tag{20}$$

This differential equation is solved by the creep function of Eq. (19). The corresponding mathematical proof can be given through the following three steps:

1. The strain history follows from insertion of Eq. (19) into Eq. (7) as
$$\varepsilon(t) = \int_{-\infty}^{t} \frac{1}{E_k}\left[1 - \exp\left(-\frac{E_k\,[t-\tau]}{\mu_k}\right)\right]\frac{\mathrm{d}\sigma}{\mathrm{d}\tau}\,\mathrm{d}\tau\,. \tag{21}$$
2. The strain rate follows from time-derivation of Eq. (21) as
$$\dot{\varepsilon}(t) = \int_{-\infty}^{t} \frac{1}{\mu_k}\,\exp\left(-\frac{E_k\,[t-\tau]}{\mu_k}\right)\frac{\mathrm{d}\sigma}{\mathrm{d}\tau}\,\mathrm{d}\tau\,. \tag{22}$$
3. Insertion of Eqs. (21) and (22) into the left-hand side of Eq. (20) delivers an expression which is identical to the right-hand side of Eq. (20), irrespective of the actual stress history, also including a stepwise stress history according to Eq. (9).

As for the sought micromechanical interpretation of the affinity parameter, let us imagine that the spring stiffnesses and dashpot viscosities of all Kelvin–Voigt elements are stress-dependent such that corresponding compliances are to be amplified by η, which is, according to Eq. (2), a function of $\sigma(t)$:

$$\frac{1}{E_k} \;\rightarrow\; \eta\,(\sigma(t)) \times \frac{1}{E_k}\,, \tag{23}$$

$$\frac{1}{\mu_k} \;\rightarrow\; \eta\,(\sigma(t)) \times \frac{1}{\mu_k}\,. \tag{24}$$

Inserting these modifications into the constitutive equation Eq. (20) yields

$$\dot{\varepsilon}(t) + \varepsilon(t)\,\frac{E_k}{\mu_k} = \frac{\sigma(t) \times \eta(\sigma(t))}{\mu_k}\,, \tag{25}$$

Eq. (25) suggests that multiplying both the spring stiffness and the dashpot viscosity with η results in a constitutive behavior of the Kelvin–Voigt unit which is equivalent to keeping the original values of the spring stiffness and of the dashpot viscosity, but multiplying the stress history with η.

Returning from the analysis of a single Kelvin–Voigt unit to the entire Prony series of many Kelvin–Voigt units, and applying the η-scaling to *all* of these Kelvin–Voigt units, but *not* to the serially arranged additional elastic spring, see the term $1/E_s$ in Eq. (18), necessitates the subdivision of the total creep function into an elastic and a viscous part, $J = J_e + J_v$. The described η-scaling of the stress applies only for the term multiplied with J_v, and not for the term multiplied with J_e. Thus, the strain solution for a stepwise stress history according to Eq. (9) takes the form

$$\varepsilon(t) = \sigma(t)\,J_e(t-t_i) + \sum_{i=1}^{n} J_v(t-t_i)\left[\sigma_i\eta_i - \sigma_{i-1}\eta_{i-1}\right]H(t-t_i)\,, \tag{26}$$

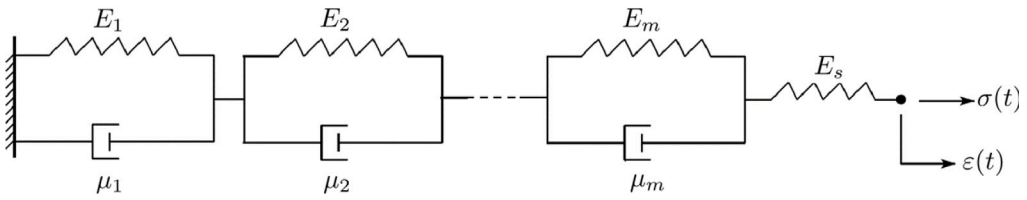

Fig. 7. Kelvin–Voigt chain used to approximate creep functions as a Prony series.

whereby $J_e = \frac{1}{E_s}$ and $J_v = \sum_{k=1}^{m} \frac{1}{E_k}\left[1 - \exp\left(-\frac{E_k[t-\tau]}{\mu_k}\right)\right]$. This is formally consistent with Eq. (16). It is concluded that the nonlinear superposition principle developed by Tasevski et al. [24] can be understood as an approach where the creep function is approximated by a Prony series and where the spring stiffnesses and dashpot viscosities of all Kelvin–Voigt units are subjected to the η-scaling of Eqs. (23) and (24). We are left with showing why the affinity concept changes the spring stiffnesses and dashpot viscosities in *all* Kelvin–Voigt units in the same way.

3.6. Kelvin–Voigt units with stress-dependent spring stiffness and dashpot viscosity: Stress-level-induced stick–slip-transition of nanoscopic viscous interfaces

A matrix-interface composite consisting of an isotropic matrix and parallel interfaces of identical size was analyzed by Shahidi et al. [37], see Fig. 8(a). Envisioning the nanoscopic interfaces to be lubricated by adsorbed water, the shear traction acting on the interfaces was set equal to their shear dislocation rate multiplied with an interface viscosity μ_{int}. Shahidi et al. [37] showed that this interface behavior manifests itself in a macroscopic (shear) stress–strain behavior of the composite which is reminiscent of the creep function given in Eq. (19).

In [39,40], the same authors extended their approach to a matrix-interface composite consisting of an isotropic matrix and k families of parallel interfaces, see Fig. 8(b). The kth family comprises interfaces with radius a_k and viscosity $\mu_{int,k}$. The interface density parameter d_k quantifies the number of interfaces of the kth family per unit volume of the studied composite. Shahidi et al. showed that the homogenized behavior of the composite can be approximated by a Prony series with one elastic spring and k Kelvin–Voigt units in a serial arrangement, and that the spring stiffness and the dashpot viscosity of the kth Kelvin–Voigt unit are functions of the interface size, viscosity, and density of the kth interface family, with the following proportionalities:

$$\frac{1}{E_k} \propto d_k \tag{27}$$

$$\frac{1}{\mu_k} \propto \frac{d_k}{a_k\, \mu_{int}}. \tag{28}$$

The extension to matrix-interface composites hosting isotropically oriented interfaces is documented in [38], see also Fig. 8(c). Such composite exhibit isotropic viscoelastic properties. Their volumetric and deviatoric creep functions are again reminiscent of a Prony series, and the proportionalities of Eq. (27) and (28) are maintained [38]. The model with isotropically oriented interfaces is well suited to study a microstructure consisting of densely packed C-S-H building blocks exhibiting isotropic orientations. Adding gel pores, capillary pores, cement grains, sand grains, and aggregates, so as to upscale the viscoelastic behavior all the way up to the material scale of concrete, does not change the kinetics of the creep behavior, because adding the five types of scale-separated pores/grains in a step-by-step fashion yields a creep behavior where stress redistributions from creeping to purely elastic constituents is very ineffective [36].

Application of the η-scaling of Eqs. (23) and (24) in Eqs. (27) and (28) shows that the affinity concept refers to a scaling of the interface density d_k, while not affecting their size a_k and viscosity μ_{int}:

$$\left.\begin{array}{lll} \frac{1}{E_k} & \rightarrow & \eta(\sigma(t)) \times \frac{1}{E_k} \\ \frac{1}{\mu_k} & \rightarrow & \eta(\sigma(t)) \times \frac{1}{\mu_k} \end{array}\right\} \quad \Leftrightarrow \quad d_k \rightarrow \eta(\sigma(t)) \times d_k\,. \tag{29}$$

Table 5
Number of microcracks detected by means of acoustic emissions during quasi-static monotonous load increase [18].

stress step	reached stress σ_i [MPa] [18]	number of microcracks created during stress step [Fig. 3]	accumulated number of microcracks
$i = 1$	24.84	396	$N_{\sigma,exp}(\sigma_1) = 396$
$i = 2$	27.14	53	$N_{\sigma,exp}(\sigma_2) = 449$
$i = 3$	33.58	546	$N_{\sigma,exp}(\sigma_3) = 995$
$i = 4$	34.50	26	$N_{\sigma,exp}(\sigma_4) = 1021$
$i = 5$	36.80	262	$N_{\sigma,exp}(\sigma_5) = 1283$

In conclusion, the idea that a higher macroscopic stress level activates a larger number of nanoscopic viscously gliding interfaces is consistent with the affinity concept for nonlinear creep [10] and the corresponding superposition principle [24]. We are left with showing that microcracking during sustained loading is (i) rather moderate within the range of applicability of the affinity concept, and (ii) significant once the limit of applicability of the affinity concept is surpassed.

4. Relations describing the creation of microcracks during a creep test

The history of acoustic emissions measured by Rossi et al. [41] entered the analysis in Section 3 as an essential input. However, such data are available in very rare cases only. This provides the motivation to derive evolution laws describing the creation of microcracks, such that the above-presented modeling approach becomes applicable also in the absence of acoustic emission measurements.

Figs. 1 and 3 underscore that microcracking progressed both during short-term loading from one stress level to the next higher one *and* during sustained loading. This is reminiscent of the historical observation that the number of microcracks at failure under quasi-static monotonous loading is significantly smaller than the number of cracks at failure under sustained loading [20,21]. Both observations suggest two classes of microcracks. The first one refers to microcracks primarily induced by the stress-to-strength ratio. Their number is denoted as N_σ. The second class refers to microcracks primarily induced by accumulated creep deformation. Their number is denoted as N_ε. Thus, the total number of microcracks can be written, at any time t, as

$$N = N_\sigma + N_\varepsilon\,. \tag{30}$$

In the following, evolution laws for both classes of microcracks are derived.

4.1. Creation of microcracks during quasi-static monotonous load increase

The data presented in Fig. 3 of [18] allows for quantifying the number of microcracks detected during the all five quasi-instantaneous stress steps. The accumulated number of these microcracks is listed in Table 5.

The relation between the accumulated number of microcracks and the stress-to-strength ratio is described by means of a power law,

$$N_\sigma(\sigma_i) = \pi_a \left[\frac{\sigma_i}{\sigma_{ult}}\right]^{\pi_b}. \tag{31}$$

The two dimensionless constants π_a and π_b are identified, for each of the three sets of realistic 266 day mechanical properties of the tested

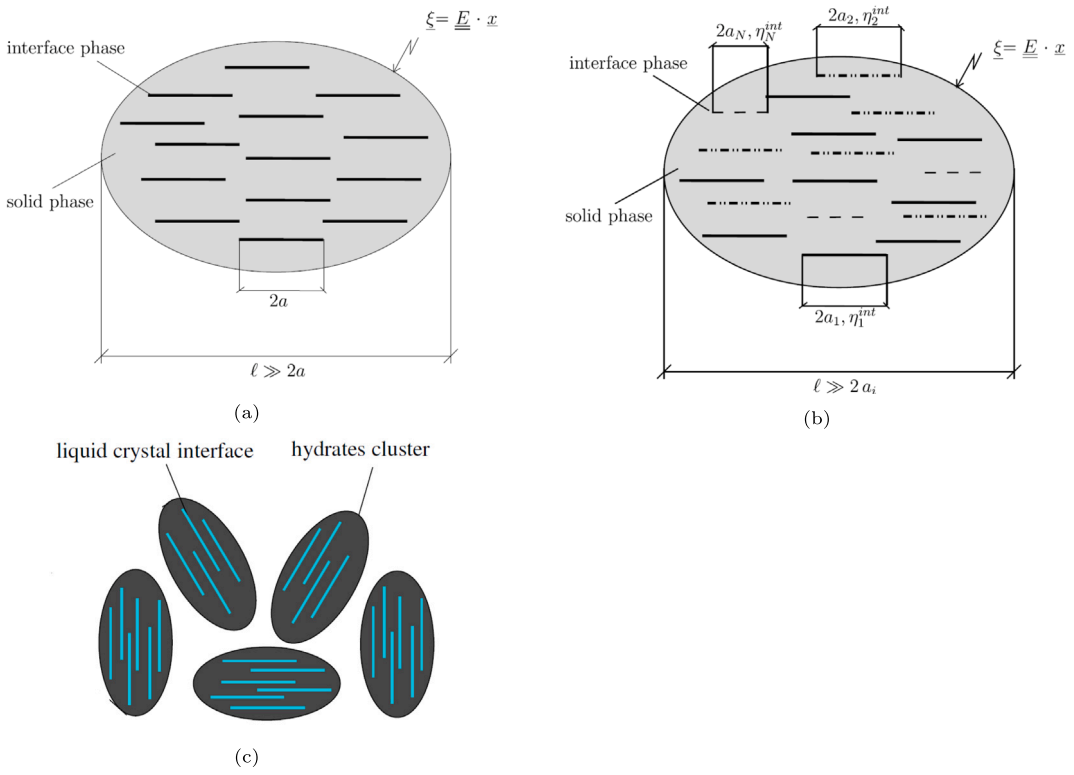

Fig. 8. Matrix-interface composite including (a) one family, and (b) N families of 2D flat spherical interfaces, oriented (a, b) parallel to each other, and (c) in an isotropic manner.

Table 6
Values of π_a and π_b according to Eq. (31) identified from the data listed in Table 5, under consideration of three different sets of the 266 day mechanical properties of the concrete tested by Rossi et al. [18], see the three values of σ_{ult} in Table 3; $k = 1, 2, 3$ refers to the uncertainty regarding the strength of the tested concrete, see also Appendix B.1.

index k [–]	$\pi_{a,k}$ [–]	$\pi_{b,k}$ [–]	root mean squared error $\mathcal{R}(\pi_{a,k}, \pi_{b,k})$ [10^{-6}]
1	2021	3	36.7
2	2240	3	36.7
3	2474	3	36.7

concrete, see the three values of σ_{ult} in Table 3, by minimizing the root mean squared difference between modeled and experimentally measured number of microcracks, i.e. the difference between N_σ according to Eq. (31) and $N_{\sigma,exp}(t)$ listed in Table 5, respectively:

$$\mathcal{R}(\pi_a, \pi_b) = \sqrt{\frac{1}{5}\sum_{i=1}^{5}\Big[N_\sigma(\pi_a, \pi_b; \sigma_i) - N_{\sigma,exp}(\sigma_i)\Big]^2} \rightarrow \min\,. \tag{32}$$

The three identified values of π_a and π_b are listed in Table 6. In all three cases, the corresponding value of $\mathcal{R}$ amounted to very satisfactory 36.7×10^{-6}. This underlines the high reproduction quality, see also Fig. 9.

4.2. Creation of microcracks during creep under sustained loading

The number of microcracks increased virtually linearly with increasing creep strain during each one of the five load plateaus of the multilevel test of Rossi et al. [18]. Therein, the following mathematical relation was used:

$$N(t) - N(t_i^+) = \alpha_i\Big(\frac{\sigma_i}{\sigma_{ult}}\Big) \times \Big[\varepsilon(t) - \varepsilon(t_i^+)\Big], \qquad t_i^+ \le t \le t_{i+1}^-\,, \tag{33}$$

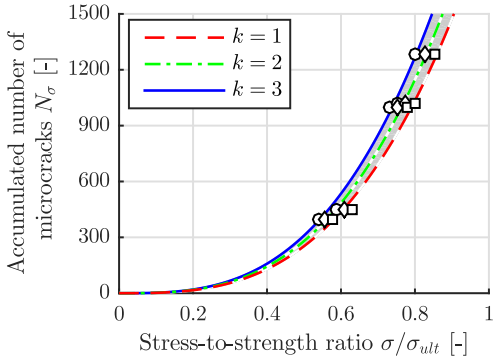

Fig. 9. Accumulated number of microcracks detected during quasi-instantaneous stress increase, see the circles and Table 5; the solid lines refer to Eqs. (31), and Table 6; $k = 1, 2, 3$ refers to the uncertainty regarding the strength of the tested concrete.

where $t_i^+ = \lim_{\epsilon \to 0}(t_i + \epsilon)$ and $t_{i+1}^- = \lim_{\epsilon \to 0}(t_{i+1} - \epsilon)$ such that $N(t_i^+)$ and $\varepsilon(t_i^+)$ refer to the number of microcracks and the strain, respectively, at the start of the load plateau during which the imposed stress is equal to σ_i, see also Figs. A.14(a)–(e). The values of the slopes α_i increase with increasing stress-to-strength ratio, see Table 7. These data serve as the basis for developing a continuous mathematical function describing the stress-dependent creation of microcracks with increasing strain on a load plateau, as explained next.

The affinity concept for nonlinear creep, which does not account explicitly for microcracks created during load plateaus, is very useful for stress-to-strength ratios up to some 70% [10]. Therefore, we envision that microcracking accompanying creep during sustained loading contributes significantly to the overall deformation at stress-to-strength ratios larger than 70%, while microcracking is of significantly smaller importance at smaller stress-to-strength ratios. In line with this expectation, and with the aim to keep the involved mathematical description

Table 7
Proportionality factor between the increase of the number of microcracks and the increase of the strain, see Eq. (33), as identified from experimental data referring to five different load plateaus, see [41] and Fig. A.14.

load plateau	stress σ_i [MPa]	slope α_i [m/μm]
$i = 1$	24.84	0.097
$i = 2$	27.14	0.267
$i = 3$	33.58	2.66
$i = 4$	34.50	6.24
$i = 5$	36.80	10.7

Table 8
Intervals of σ/σ_{ult} and corresponding values of the dimensionless coefficients π_c and π_d of Eq. (34).

interval of stress-to-strength ratio					constants of Eq. (34)	
		$\frac{\sigma}{\sigma_{ult}}$	$\leq$	$(\sigma/\sigma_{ult})_I$:	$\pi_c = 0$,	$\pi_d = 0$,
$(\sigma/\sigma_{ult})_I$	$\leq$	$\frac{\sigma}{\sigma_{ult}}$	$\leq$	$(\sigma/\sigma_{ult})_{II}$:	$\pi_c = \pi_{c,low}$,	$\pi_d = \pi_{d,low}$,
$(\sigma/\sigma_{ult})_{II}$	$\leq$	$\frac{\sigma}{\sigma_{ult}}$:			$\pi_c = \pi_{c,high}$,	$\pi_d = \pi_{d,high}$.

Table 9
Values of π_c and π_d according to Eq. (34) identified from the data listed in Table 7, under consideration of three different sets of the 266 day mechanical properties of the concrete tested by Rossi et al. [18], see the three values of σ_{ult} in Table 3; and limits of applicability of the identified values of π_c and π_d, see also Table 8; $k = 1, 2, 3$ refers to the uncertainty regarding the strength of the tested concrete, see also Appendix B.1.

index k	$(\sigma/\sigma_{ult})_{I,k}$ [–]	$\pi_{c,low,k}$ [10^6]	$\pi_{d,low,k}$ [10^6]	$(\sigma/\sigma_{ult})_{II,k}$ [–]	$\pi_{c,high,k}$ [10^6]	$\pi_{d,high,k}$ [10^6]
1	0.55	3.178	−1.739	0.76	102.8	−77.01
2	0.53	3.289	−1.739	0.73	106.3	−77.01
3	0.51	3.400	−1.739	0.71	109.9	−77.01

reasonably simple, the relation between the slope α and the stress-to-strength ratio σ/σ_{ult} is modeled as a piecewise linear function. Every piece is expressed as:

$$\alpha = \pi_c \left[\frac{\sigma}{\sigma_{ult}}\right] + \pi_d\,, \tag{34}$$

see also Table 8.

The first linear relation is established for stress-to-strength ratios *within* the range of applicability of the affinity concept. To this end, the dimensionless coefficients π_c and π_d are identified such that Eq. (34) delivers a function running through the two pairs of values α_i and σ_i/σ_{ult}, referring to the first and the second load plateau of Rossi et al.'s multistage test ($i = 1, 2$), see Table 7. The identification is performed three times, noting that there are three sets of realistic 266 day mechanical properties of the tested concrete, see the three values of σ_{ult} in Table 3. This yields the values of $\pi_{c,low}$ and $\pi_{d,low}$ listed in Table 9, see also the linear graphs with the smaller inclination in Fig. 10. These graphs intersect the abscissa at $\sigma/\sigma_{ult} = (\sigma/\sigma_{ult})_I \approx 51\% - 55\%$.

The second linear relation is established for stress-to-strength ratios *beyond* the limit of applicability of the affinity concept. To this end, the dimensionless coefficients π_c and π_d are identified such that Eq. (34) delivers the best regression function for the three pairs of values α_i and σ_i/σ_{ult}, referring to the third, the fourth, and the fifth load plateau of Rossi et al.'s multistage test ($i = 3, 4, 5$), see Table 7. The identification is performed three times, noting that there are three sets of realistic 266 day mechanical properties of the tested concrete, see the three values of σ_{ult} in Table 3. This yields the values of $\pi_{c,high}$ and $\pi_{d,high}$ listed in Table 9, see also the linear graphs with the larger inclination in Fig. 10. These steeper graphs intersect the less steeper ones of the first linear relation at $\sigma/\sigma_{ult} = (\sigma/\sigma_{ult})_{II} \approx 71\% - 76\%$.

The identified values $(\sigma/\sigma_{ult})_I$ and $(\sigma/\sigma_{ult})_{II}$ imply three conclusions: (i) Virtually no microcracking occurs at stress-to-strength ratios up to $(\sigma/\sigma_{ult})_I \approx 51\%-55\%$, as expressed by $\pi_c = \pi_d = 0\,\text{m/μm}$; (ii) creep under sustained loading will be accompanied by *moderate* microcracking in the interval of stress-to-strength ratios from $(\sigma/\sigma_{ult})_I \approx 51\%-55\%$ to $(\sigma/\sigma_{ult})_{II} \approx 71\% - 76\%$; (iii) *significant microcracking* occurs beyond the limit of applicability of the affinity concept, i.e. in the range of stress-to-strength ratios larger than $(\sigma/\sigma_{ult})_{II} \approx 71\% - 76\%$, see also Table 8.

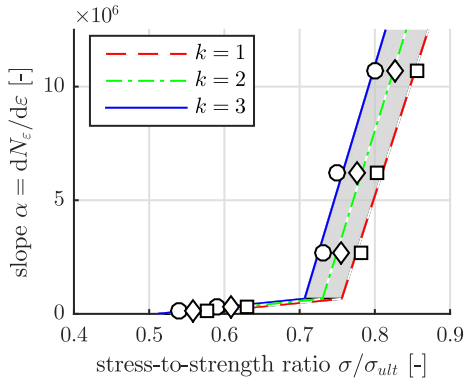

Fig. 10. Relation between slope of the linear relations between the total time-dependent strain and the stress-to-strength ratio; $k = 1, 2, 3$ refers to the uncertainty regarding the strength of the tested concrete.

4.3. Prediction of creation of microcracks during sustained loading

As for modeling the creation of microcracks during the ith load plateau, $\varepsilon(t)$ from Eq. (16) is inserted into Eq. (33). This yields:

$$\begin{aligned} N(t) - N(t_i^+) = \alpha_i \Bigg\{ & \left[1 + \gamma^3 \frac{N(t)}{V}\right] \left[\frac{\sigma(t)}{E} \right. \\ & \left. + \sum_{j=1}^{i} \left[\sigma_j \eta_j - \sigma_{j-1}\eta_{j-1}\right] \frac{RH}{E_c} \left[\frac{t - t_j}{t_{ref}}\right]^{\beta} H(t - t_j) \right] \\ & - \left[1 + \gamma^3 \frac{N(t_i^+)}{V}\right] \left[\frac{\sigma(t_i^+)}{E} \right. \\ & \left. + \sum_{j=1}^{i} \left[\sigma_j \eta_j - \sigma_{j-1}\eta_{j-1}\right] \frac{RH}{E_c} \left[\frac{t_i^+ - t_j}{t_{ref}}\right]^{\beta} H(t_i - t_j) \right] \Bigg\}, \\ & t_i^+ \leq t \leq t_{i+1}^-\,, \end{aligned} \tag{35}$$

which is an implicit expression for $N(t)$. Under consideration of the abbreviation

$$\varepsilon(t, \gamma{=}0) = \frac{\sigma(t)}{E} + \sum_{j=1}^{i} \left[\sigma_j \eta_j - \sigma_{j-1}\eta_{j-1}\right] \frac{RH}{E_c} \left[\frac{t - t_j}{t_{ref}}\right]^{\beta} H(t - t_j) \tag{36}$$

and of $\left[1 + \gamma^3 \frac{N(t_i)}{V}\right] \varepsilon(t_i^+, \gamma = 0) = \varepsilon(t_i^+)$, where $\varepsilon(t_i^+)$ refers to Eq. (16) evaluated for $t = t_i^+$, Eq. (35) is solved for the number of microcracks $N(t)$:

$$N(t) = \frac{N(t_i^+) + \alpha_i \left[\varepsilon(t, \gamma{=}0) - \varepsilon(t_i^+)\right]}{1 - \frac{\alpha_i \gamma^3}{V} \varepsilon(t, \gamma{=}0)}\,, \qquad t_i^+ \leq t \leq t_{i+1}^-\,. \tag{37}$$

The increment of microcracks created in the time interval from t_i^+ to t is denoted as $\Delta N_i(t)$. It is equal to $N(t) - N(t_i^+)$ and follows as:

$$\Delta N_i(t) = \frac{N(t_i^+) + \alpha_i \left[\varepsilon(t, \gamma{=}0) - \varepsilon(t_i^+)\right]}{1 - \frac{\alpha_i \gamma^3}{V} \varepsilon(t, \gamma{=}0)} - N(t_i^+)\,, \qquad t_i^+ \leq t \leq t_{i+1}^- \tag{38}$$

Re-arranging terms in Eq. (38) yields

$$\Delta N_i(t) = \frac{\alpha_i \left\{ \left[1 + \frac{\gamma^3 N(t_i^+)}{V}\right] \varepsilon(t, \gamma{=}0) - \varepsilon(t_i^+) \right\}}{1 - \frac{\alpha_i \gamma^3}{V} \varepsilon(t, \gamma{=}0)}\,, \qquad t_i^+ \leq t \leq t_{i+1}^- \tag{39}$$

The number of microcracks accumulating during (i) the load plateau of a single-stage creep test and (ii) the 1st load plateau of a multi-stage creep test follows from inserting $i = 1$ into Eq. (39) as:

$$N_\varepsilon(t) = \frac{\alpha_1 \left\{ \left[1 + \frac{\gamma^3 N(t_1^+)}{V}\right] \varepsilon(t, \gamma = 0) - \varepsilon(t_1^+) \right\}}{1 - \frac{\alpha_1 \gamma^3}{V} \varepsilon(t, \gamma = 0)}, \qquad t_1^+ \le t \le t_2^- . \tag{40}$$

The number of microcracks accumulating from the start of the ith load plateau at time t_i^+ to the end of this load plateau at time t_{i+1}^- follows from inserting $t = t_{i+1}^-$ in Eq. (39) and reads as:

$$\Delta N_i(t_{i+1}^-) = \frac{\alpha_i \left\{ \left[1 + \frac{\gamma^3 N(t_i^+)}{V}\right] \varepsilon(t_{i+1}^-, \gamma = 0) - \varepsilon(t_i^+) \right\}}{1 - \frac{\alpha_i \gamma^3}{V} \varepsilon(t_{i+1}^-, \gamma = 0)}, \qquad t_i^+ \le t \le t_{i+1}^- \tag{41}$$

The number of microcracks accumulating in a multistage creep test, during all the load plateaus until time t during the ith load plateau ($i > 1$) can be expressed as

$$N_\varepsilon(t) = \Delta N_i(t) + \sum_{j=1}^{i-1} \Delta N_j(t_{j+1}^-), \qquad t_i^+ \le t \le t_{i+1}^-, \qquad i > 1 . \tag{42}$$

Inserting Eqs. (39) and (41) into Eq. (42) finally yields

$$N_\varepsilon(t) = \frac{\alpha_i \left\{ \left[1 + \frac{\gamma^3 N(t_i^+)}{V}\right] \varepsilon(t, \gamma = 0) - \varepsilon(t_i^+) \right\}}{1 - \frac{\alpha_i \gamma^3}{V} \varepsilon(t, \gamma = 0)} + \sum_{j=1}^{i-1} \frac{\alpha_j \left\{ \left[1 + \frac{\gamma^3 N(t_j^+)}{V}\right] \varepsilon(t_{j+1}^-, \gamma = 0) - \varepsilon(t_j^+) \right\}}{1 - \frac{\alpha_j \gamma^3}{V} \varepsilon(t_{j+1}^-, \gamma = 0)}, \qquad t_i^+ \le t \le t_{i+1}^-, \qquad i > 1 . \tag{43}$$

4.4. Creation of microcracks during single-stage and multi-stage creep tests

The number of microcracks, created up to time t during the 1st stress level σ_1, follows from inserting N_σ according to Eq. (31) and N_ε according to Eq. (40) into Eq. (30) as

$$N(t) = \pi_a \left[\frac{\sigma_1}{\sigma_{ult}}\right]^{\pi_b} + \frac{\alpha_1 \left\{ \left[1 + \frac{\gamma^3 N(t_1^+)}{V}\right] \varepsilon(t, \gamma = 0) - \varepsilon(t_1^+) \right\}}{1 - \frac{\alpha_1 \gamma^3}{V} \varepsilon(t, \gamma = 0)}, \qquad t_1^+ \le t \le t_2^- \tag{44}$$

The number of microcracks, created up to time t during the ith stress level σ_i, with $i > 1$, follows from inserting N_σ according to Eq. (31) and N_ε according to Eq. (43) into Eq. (30) as

$$N(t) = \pi_a \left[\frac{\sigma_i}{\sigma_{ult}}\right]^{\pi_b} + \frac{\alpha_i \left\{ \left[1 + \frac{\gamma^3 N(t_i^+)}{V}\right] \varepsilon(t, \gamma = 0) - \varepsilon(t_i^+) \right\}}{1 - \frac{\alpha_i \gamma^3}{V} \varepsilon(t, \gamma = 0)} + \sum_{j=1}^{i-1} \frac{\alpha_j \left\{ \left[1 + \frac{\gamma^3 N(t_j^+)}{V}\right] \varepsilon(t_{j+1}^-, \gamma = 0) - \varepsilon(t_j^+) \right\}}{1 - \frac{\alpha_j \gamma^3}{V} \varepsilon(t_{j+1}^-, \gamma = 0)}, \qquad t_i^+ \le t \le t_{i+1}^-, \quad i > 1 . \tag{45}$$

Eqs. (44) and (45) allow for computing the number of microcracks created in concrete volumes V subjected either to single-stage or multi-stage creep tests. This enables the analysis of creep tests without accompanying acoustic emission experiments.

The predictive capability of Eqs. (44) and (45) will be checked in the following section. Thereby, π_a and π_b according to Table 6, α according to Eq. (34), π_c and π_d according to Tables 8 and 9, will be taken as constants. The damage factor γ, in turn, cannot be assumed to be the same for all concretes, given that it accounts for the orientational properties of the microcrack network and for the size of the microcracks, see Eq. (13). The size of microcracks is likely the larger, the larger the maximum aggregate size.

5. Model validation

5.1. Prediction of strain histories measured by Rossi et al. [41] in two single-step creep tests

The developed nonlinear creep model of Eq. (16) together with the microcrack evolution law according to Eq. (44) is used to predict the strain histories of two single-step compressive creep tests presented in [41]. The tested concrete is nominally the same as the one subjected to the already analyzed multi-stage creep test of [18]. Still, the specimens of the two different studies [18,41] were produced in two different batches.

The first single-step creep test of [41] was started at a material age of 28 days. The strength at that time amounted to 39.9 MPa. The stress imposed during creep testing amounted to 13.6 MPa, see Table 10. Because the stress-to-strength ratio was equal to 34%, this test is useful to check whether or not the *linear* creep properties of the material are accurately predicted.

The second single-step creep test of [41] was started at a material age of 145 days. The strength at that time amounted to 47.2 MPa, see Appendix B.2. The stress imposed during creep testing amounted to 33 MPa, see Table 10. Because the stress-to-strength ratio was equal to 70%, this test is useful to check whether or not the nonlinear creep properties of the material are accurately predicted, including the combination of nonlinear viscoelastic phenomena and microcracking.

The material properties required for evaluation of Eq. (16) are listed in Table 10. They were obtained as follows. The hydration degrees ξ were identified by means of the validated multiscale model of [43] from the strength values reported above, the initial water-to-cement mass ratio w/c, and the initial aggregate-to-cement mass ratio a/c. Values of the elastic modulus and the creep modulus of concrete were quantified by means of the multiscale model of [44,63], using the given values of w/c, a/c, and ξ together with the elastic modulus of the aggregates of $E_{agg} = 45$ GPa. The internal relative humidity was estimated by interpolation between measurements documented in [45].

The damage factor γ refers to the microcracks developing during a uniaxial creep tests. It is expectable that the size of these microcracks is the larger, the larger the maximum aggregate size. Given that the concrete of the two single-step creep tests was nominally the same as the one of the multi-stage creep test, including the same aggregate type and size distribution, it is concluded that γ-values identified from the multi-stage creep test apply also to the single-step creep tests.

Three predictions ($k = 1, 2, 3$) are computed for each one of the two single-step creep tests. They refer to the three values of γ, π_a, π_b, π_c, and π_d as listed in Tables 4, 6, and 9. These sets of three values reflect the uncertainty of the maturity of the concrete subjected to the multi-stage creep test. The *a priori* knowledge of all input quantities required for evaluation of Eqs. (16) and (44) allows for predicting the experimental results, i.e. there is no need to identify/optimizing any input values. A very accurate prediction was achieved both in the linear and nonlinear creep domain, see the bottom circles and the top circles, respectively, Fig. 11. Remarkably, the blue and green graphs, referring to $k = 2$ and $k = 3$ in Tables 4, 6, and 9, run very close to the measured data. This shows that the nonlinear creep model performs well both in the linear and nonlinear creep regimes, and that the damage factor γ may be assumed as constant, at least as long as the properties of the aggregates are the same.

Table 10
Input properties for the simulation of strain histories in different basic creep tests; $k = 1,2,3$ refers to the uncertainty regarding the strength of the tested concrete, see also Appendices B.1 and B.2.

Property		Rossi (2012) [18]	Rossi (2013) [41]	Kammouna [27]
Cement type		CEM I 52.5 N	CEM I 52.5 N	CEM I B 52.5
initial water-to-cement mass ratio w/c [–]		0.54	0.54	0.50
initial aggregate-to-cement mass ratio a/c [–]		5.33	5.33	5.22
Elastic modulus of aggregates E_{agg} [GPa]		45	45	45
Maximum aggregate size $\max d_{agg}$ [mm]		20	20	8
Volume of specimens V [m^3]		0.0201	0.0201	0.0005
Material age at start t_0 [days]		266	28 | 145	90
Internal relative humidity RH [–]		95%	98% | 95%	96%
Stress applied σ [MPa]		24.9 … 36.8	13.6 | 33.0	26.4 | 42.2
	Strength $\sigma_{ult,1}$	43	39.9 | 47.2	49.7
	Hydration degree ξ_1 [–]	0.84	0.81 | 0.89	0.85
$k = 1$	Elastic modulus E_1 [GPa]	30.9	30.1 | 31.8	32.7
	Creep modulus $E_{c,1}$ [GPa]	190.2	178.6 | 204.5	223.4
	γ_1 [mm]	11.7	11.7	1.9
	Strength $\sigma_{ult,2}$	44.5	39.9 | 47.2	52.7
	Hydration degree ξ_2 [–]	0.86	0.81 | 0.89	0.88
$k = 2$	Elastic modulus E_2 [GPa]	31.2	30.1 | 31.8	33.2
	Creep modulus $E_{c,2}$ [GPa]	195.4	178.6 | 204.5	233.5
	γ_2 [mm]	12.7	12.7	4.5
	Strength $\sigma_{ult,3}$	46	39.9 | 47.2	55.7
	Hydration degree ξ_3 [–]	0.88	0.81 | 0.89	0.91
$k = 3$	Elastic modulus E_3 [GPa]	31.5	30.1 | 31.8	33.7
	Creep modulus $E_{c,3}$ [GPa]	200.7	178.6 | 204.5	242.7
	γ_3 [mm]	13.6	13.6	3.0

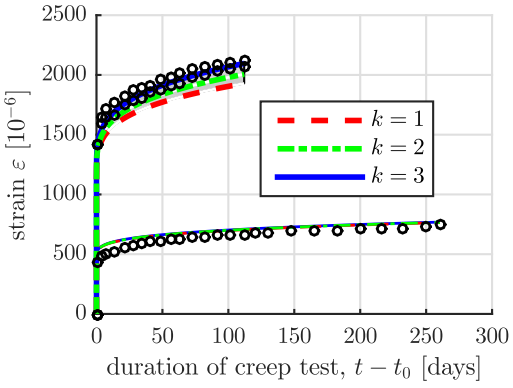

Fig. 11. Prediction of the compressive strain evolution in the single-step basic creep tests by Rossi et al. [41] based on Eqs. (16) and (44), evaluated for material properties taken from Table 10: the red, green, and blue graphs refer to $k = 1,2,3$ in Tables 4, 6, and 9; and independently measured strains, see the circles; $k = 1,2,3$ refers to the uncertainty regarding the strength of the tested concrete, see also Appendix B.2. (For interpretation of the references to color in this figure legend, the reader is referred to the web version of this article.)

5.2. Model application to strain histories measured by Kammouna et al. [27] in two single-step creep tests

The developed nonlinear creep model of Eq. (16) together with the microcrack evolution law according to Eq. (44) is used for the analysis of two basic creep tests performed by Kammouna et al. [27]. Both single-step creep tests were started at a material age of 90 days. Corresponding cylinder compressive strength values were determined from crushing control specimens. The average strength amounted to $\sigma_{ult} = 52.7$ MPa. The scatter in the measured strength values provides the motivation to investigate three scenarios, namely the mean strength plus/minus $\Delta\sigma_{ult} = 3$ MPa, that is $\sigma_{ult,1} = 49.7$ MPa, $\sigma_{ult,2} = 52.7$ MPa, and $\sigma_{ult,3} = 55.7$ MPa, see Table 10.

The stress imposed during the two creep test amounted to 26.4 MPa and to 42.2 MPa, respectively, see Table 10. Thus, the stress-to-strength ratio was equal to some 50% and to some 80%, respectively. These tests are useful to check whether or not the *nonlinear* creep properties of the material are accurately predicted in the regimes of moderate and of significant microcracking during sustained loading.

Values of the hydration degree, the elastic modulus, the creep modulus, and the internal relative humidity are listed in Table 10. They were determined as follows. Values of $\sigma_{ult,k}$, w/c, and a/c are translated by means of [43] into values of ξ_k. Values of ξ_k, w/c, a/c, and E_{agg} are translated by means of [44,63] into values of E_k and $E_{c,k}$. The internal relative humidity of the concrete at the time of testing is estimated based on [45].

Each one of the two tests is analyzed three times, motivated by the three different strength values given above ($k = 1,2,3$). The latter are combined with the corresponding microcrack evolution laws for (i) short term loading, see Eq. (31), Table 6, and Fig. 9, as well as (ii) sustained loading, see Eqs. (33) and (34), Tables 8 and 9, and Fig. 10. Thus, there is only one unknown left: the damage factor γ. It is optimized following the approach used in Section 3.4. The resulting values γ_k with $k = 1,2,3$ are listed in Table 10. The developed model, together with the newly identified values of the damage factor γ, reproduces both tests very accurately, see Fig. 12.

6. Discussion

6.1. Significance of microcracking during sustained loading at stress-to-strength ratios beyond the limit of applicability of the affinity concept

The developed model explicitly accounts for microcracking during both quasi-instantaneous load application *and* sustained loading.

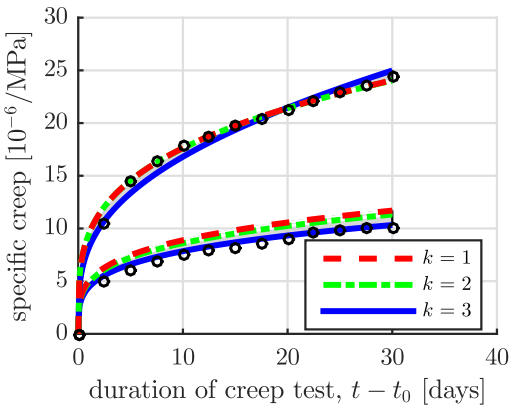

Fig. 12. Simulation of the compressive strain evolution in the single-step basic creep tests by Kammouna et al. [27] based on Eqs. (16) and (44), evaluated for material properties taken from Table 10: the red, green, and blue graphs refer to $k = 1, 2, 3$ in Tables 6 and 9; and independently measured strains, see the circles; $k = 1, 2, 3$ refers to the uncertainty regarding the strength of the concrete tested in [18], see also Appendix B.1. (For interpretation of the references to color in this figure legend, the reader is referred to the web version of this article.)

The affinity model of Ruiz et al. [10], in turn, implicitly accounts for microcracking during quasi-instantaneous load application, while microcracking during sustained loading is disregarded, see Eq. (1). In order to demonstrate the significance of microcrack creation during sustained loading at stress-to-strength ratios beyond the limit of applicability of the affinity concept, the developed model is once again employed for the simulation of the basic creep tests from [18], [41], and [27], but this time N_ε is set equal to zero, i.e. the new simulations account for microcracking during quasi-instantaneous load application but disregard microcracking during sustained loading, see Fig. 13. These additional simulations significantly underestimate the strains measured during (i) the third load level of the multi-stage creep test of [18], see Fig. 13(a), (ii) the single-step creep test of [41], performed under $\sigma = 33$ MPa, see Fig. 13(b), and (iii) the single-step creep test of [27], performed under $\sigma = 42.2$ MPa, see Fig. 13(c).

6.2. Micromechanical interpretation of the newly introduced damage factor γ

The damage factor γ accounts for orientational properties of the microcrack network and for the size of the microcracks, see Eq. (13). The values of γ are expected to decrease with decreasing values of $\max d_{agg}$. Therefore, γ is to be identified for every specific concrete of interest. And indeed, the γ-values of the concrete tested by Rossi et al. [18,41], with $\max d_{agg} = 20$ mm, are larger than the γ-values of the concrete tested by Kammouna et al. [27], with $\max d_{agg} = 8$ mm, see Table 10.

The strength of the concretes tested by Rossi et al. [18] and by Kammuna et al. [27] is uncertain. Three reasonable strength values per creep tests study have been the basis for the presented analyses. Uncertainty propagation has led to related sets of reasonable values of the degree of hydration, of the elastic modulus, of the creep modulus, and, finally of the damage factor. The labels $k = 1, 2, 3$ used in Figs. 6 and 9 to 13 as well as in Tables 3, 4, 6, 9, and 10 refer to this uncertainty propagation. Even tough this uncertainty exists, solid conclusions can be drawn on mechanisms governing the nonlinear compressive creep behavior of concrete. Before presenting these conclusions, the limitations of the present study are discussed.

6.3. Limitations

The proposed continuum damage approach is reasonable as long as microcracking occurs disorderly throughout the specimen, while microcrack *localization* is beyond the limit of applicability. Notably, localization of microcracking occurs either (i) close to the peak load in a uniaxial compressive strength test [50], or (ii) in the tertiary regime of a high-stress creep test, in which the macroscopic strain rate *increases* with increasing time, leading to failure under sustained loading. In all cases of time-invariant loading analyzed herein, however, the macroscopic strain rate *decreases* with increasing time. This is outside the tertiary creep regime, and the assumption of diffuse microcracking is reasonable, such that the presented model was operated within its limit of applicability.

Given that localization of microcracking is beyond the limit of applicability of the presented model, its adaptation to *tension-dominated* exposure conditions appears to be out of reach, because tension promotes microcrack localization, see e.g. bending experiments on unnotched or notched prisms [69]. In bending creep tests ending with failure under sustained load, tensile microcracking (i) is detected in the primary creep regime, shortly after the load application, (ii) vanishes during the subsequent secondary creep regime, where measured deformation increases virtually linearly with increasing time, and (iii) starts again in the tertiary phase of creep, where microcracking clearly corresponds to the growth of damage prior to failure [70]. When subjecting unnotched and notched concrete beams to three point bending tests with *monotonous* load increase up to failure, smaller microcracks with higher frequencies are dominantly generated up to the vicinity of the peak load, while larger fractures with lower frequency are observed near the peak load and in the post-peak [71]. These observations imply that the characteristic energetic "signature" of the population of acoustic events changes during testing, and this change is likely related to the transition from well distributed microcrack nucleation further away from the peak load, to propagation of already formed microcracks resulting in crack coalescence close to the peak load. Modeling of localization phenomena calls for more advanced simulation techniques, such as nonlocal or discrete lattice models [72,73]. The latter provide motivation for introducing an internal length in continuum damage formulations [74], i.e. a correlation length owing to spatial redistributions and interactions during the failure process. This length varies with system size and increases with increasing damage [73].

Additional limitations of the presented study refer to its scope. It was focused on creep of mature concrete made from ordinary Portland cement, under constant moisture, maturity, and temperature. The extension to other cement chemistries, early-age creep, drying and/or wetting, aging, and variable temperatures are topics for future research.

7. Conclusions

The developed model for nonlinear creep of concrete is an extension of the affinity concept toward consideration of microcracking during sustained loading. From the results of the presented study, it is concluded that:

- there are two mechanisms governing nonlinear compressive creep of concrete:
  1. stress-induced activation (stick–slip transition) of gliding viscous interfaces, at the nanostructure of cement paste;
  2. microcracking during sustained loading, at a rate which is virtually proportional to the strain rate, with a proportionality factor that increases bilinearly with increasing stress-to-strength ratio;
- mechanism 1, which leads to nonlinear viscoelastic behavior, was identified herein by means of micromechanics relations between Kelvin–Voigt-type rheological models for creep of concrete and viscous shear-sliding of nanoscopic interfaces lubricated by confined water; it is phenomenologically accounted for by the affinity concept for nonlinear creep, see Eqs. (1) and (2);

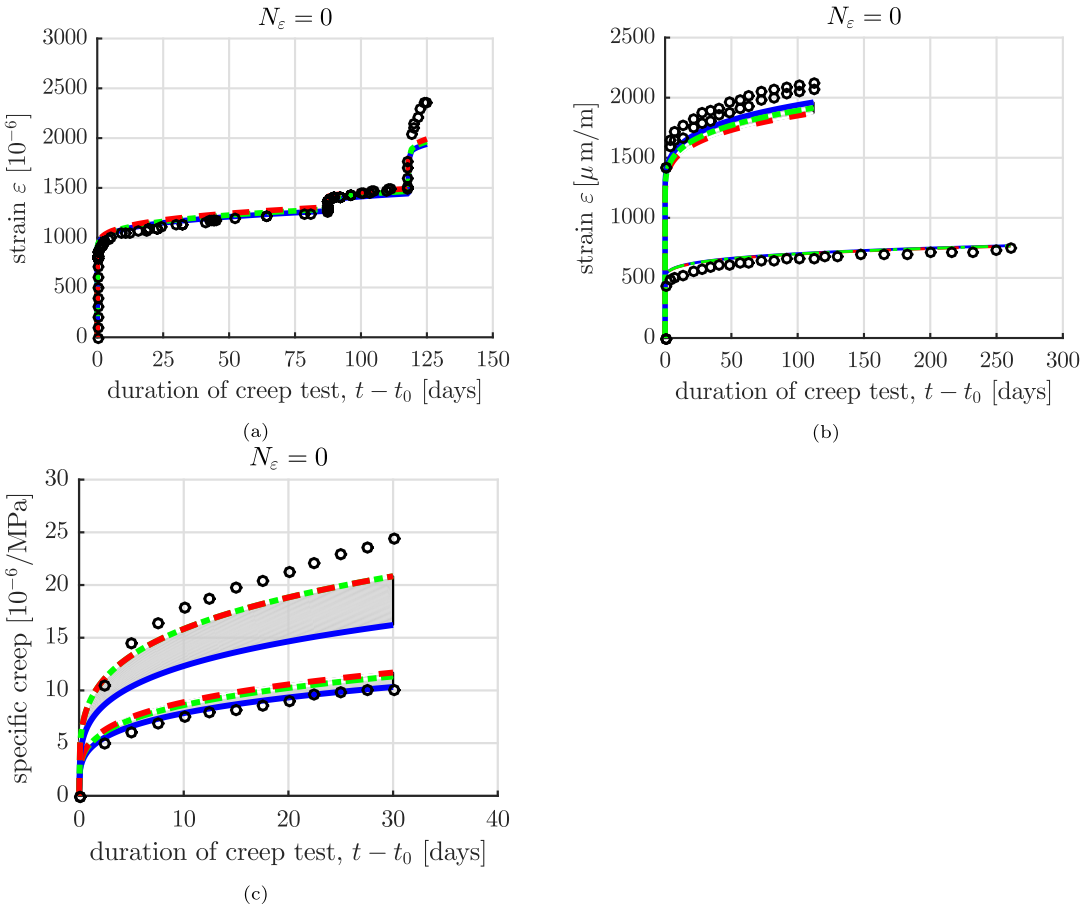

Fig. 13. Simulation (blue, red, and green lines) of the basic creep tests from (a) Rossi et al. [18], (b) Rossi et al. [41], and (c) Kammouna et al. [27], while accounting for microcracking during quasi-instantaneous load application but without accounting for microcracking during sustained loading; $k = 1, 2, 3$ refers to the uncertainty regarding the strength of concrete. (For interpretation of the references to color in this figure legend, the reader is referred to the web version of this article.)

- mechanism 2, which leads to damage of concrete, was identified herein by means of micromechanical relations between the damage-induced increase of the compliance of concrete and the creation of distributed microcracks during sustained loading; it is of minor importance in the regime of stress-to-strength smaller than some 50%, of moderate importance in the regime of stress-to-strength between some 50% and some 70%, and of major importance beyond;
- the number of microcracks created during both short-term load application and sustained loading is directly proportional to damage of concrete, provided that a micromechanics-inspired damage model is formulated, in which (i) the number of microcracks is directly proportional to the damage variable, and (ii) the damage variable linearly increases the *compliance* (= the *inverse* of the stiffness) of the material;
- the demonstrated model performance underlines that the newly introduced damage factor γ is the larger, the larger the maximum aggregate size. Still, the value of γ is *independent* of the applied stress level, i.e. independent of the stress-to-strength ratio, and *the same* value of γ can be used for microcracks generated during both short-term load application *and* during sustained loading.

CRediT authorship contribution statement

Rodrigo Díaz Flores: Writing – original draft, Validation, Software, Investigation, Formal analysis. **Christian Hellmich:** Writing – review & editing, Supervision, Methodology, Funding acquisition. **Bernhard Pichler:** Writing – review & editing, Writing – original draft, Supervision, Methodology, Funding acquisition, Conceptualization.

Funding

This research received financial support by the Austrian Research Promotion Agency (FFG) within the COMET project #882504 "Rail4Future: Resilient Digital Railway Systems to enhance performance".

Declaration of competing interest

The authors declare that they have no known competing financial interests or personal relationships that could have appeared to influence the work reported in this paper.

Acknowledgment

The authors acknowledge the TU Wien University Library for financial support through its Open Access Funding Programme.

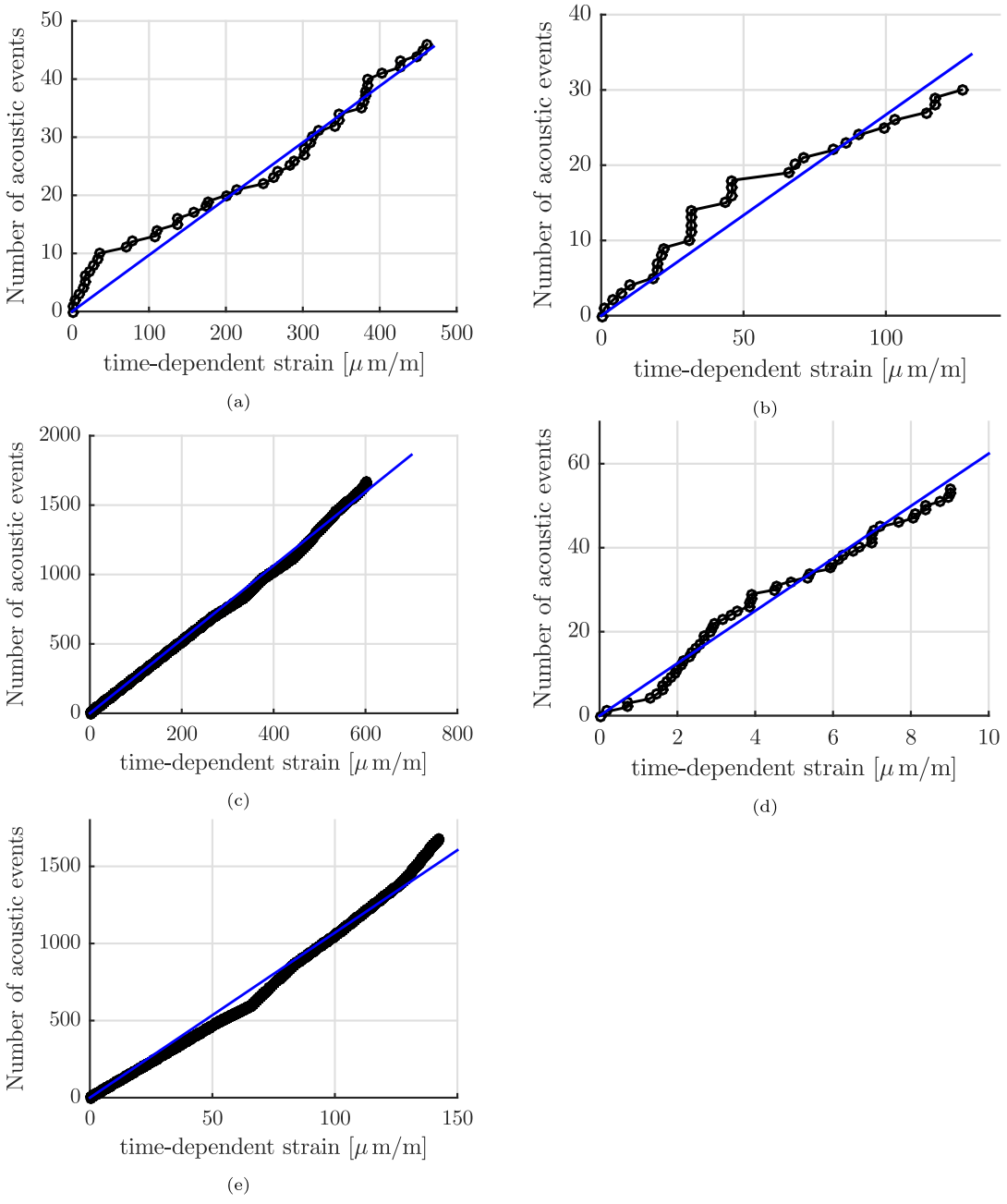

Fig. A.14. Number of acoustic events as a function of the time-dependent strain for the stress-to-strength ratios of (a) 54%, (b) 59%, (c) 73%, (d) 75%, and (e) 80%.

Appendix A. Number of acoustic events during load plateaus, N_ϵ, as a function of the time-dependent strain

Figs. A.14(a)–A.14(e) show the number of acoustic events as a function of the total time-dependent strain, as experimentally obtained in Figs. 4–8 of [18].

Appendix B. Estimation of the compressive strength at the age of loading for each test

B.1. Multi-step test by Rossi et al. [18]

The strength of concrete at the age of 266 days, $\sigma_{ult,266d}$, is estimated based on the 28 day cube compressive strength [18], see Eq. (3), and cylinder strength values of nominally identical concrete, determined at material ages amounting to 7, 14, 28, 64, 90, and 180 days [41], see Fig. B.15.

As for the first estimate, Table 5.1-3 of the fib Model Code [42] is used to convert the 28 day cube compressive strength into the mean value of the 28 day compressive strength. The obtained result, $\sigma_{ult,28d} = 37.4\,\text{MPa}$, is extrapolated to 266 days based on Eq. (5.1-50) of [42]:

$$\sigma_{ult}(t) = \sigma_{ult,28d}\,\exp\left[s\left(1-\sqrt{\frac{28\,\text{days}}{t}}\right)\right]. \tag{B.1}$$

Evaluation of Eq. (B.1) for $s = 0.20$, which is recommended for the used strength class of cement [42], and for $t = 266\,\text{days}$ yields:

$$\sigma_{ult} = 43.0\,\text{MPa}\,. \tag{B.2}$$

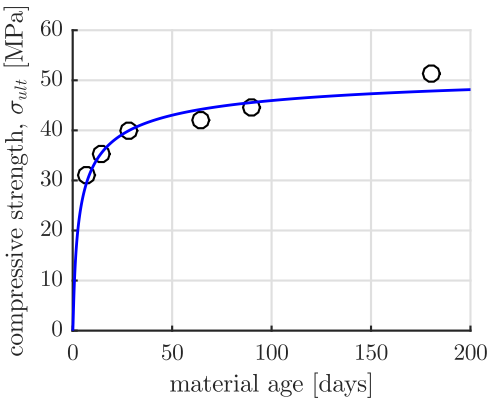

Fig. B.15. Evolution of strength as a function of time for the concrete tested by Rossi et al. [41]. The blue curve refers to the use of Eq. (B.1) with the optimized value of $s = 0.30$. (For interpretation of the references to color in this figure legend, the reader is referred to the web version of this article.)

As for the second estimate, the s-value in Eq. (B.1) is optimized such as to best reproduce the strength evolution of the nominally identical concrete. This is inspired by Ausweger et al. [75], who showed that most realistic s-values might deviate from the recommendations of the fib Model Code. And indeed, the measured strength evolution is best reproduced when using $s = 0.30$, see Fig. B.15. Inserting this value together with $t = 266\,\text{days}$ into (B.1) yields:

$$\sigma_{ult} = 46.0\,\text{MPa}\,. \tag{B.3}$$

The third estimate is simply the average of the first two estimates, see Eqs. (B.2) and (B.3):

$$\sigma_{ult} = 44.5\,\text{MPa}\,. \tag{B.4}$$

B.2. Single-step tests by Rossi et al. [41]

The compressive strength of the tested concrete was obtained using cylindrical samples at material ages of 7 days, 14 days, 28 days, 64 days, 90 days, and 180 days. As regards the creep test performed at an age of 28 days, the strength measured at that same age was used: $\sigma_{ult,28d} = 39.9\,\text{MPa}$. As regards the creep test performed at an age of 145 days, Eq. (B.1) and Fig. B.15 were used to interpolate between measured data, yielding a value of $\sigma_{ult,145d} = 47.2\,\text{MPa}$.

Data availability

No data was used for the research described in the article.

References

[1] S. Ullah, B. Pichler, S. Scheiner, C. Hellmich, Influence of shotcrete composition on load-level estimation in NATM-tunnel shells: Micromechanics-based sensitivity analyses, Int. J. Numer. Anal. Methods Geomech. 36 (9) (2012) 1151–1180.

[2] R. Scharf, B. Pichler, R. Heissenberger, B. Moritz, C. Hellmich, Data-driven analytical mechanics of aging viscoelastic shotcrete tunnel shells, Acta Mech. 233 (8) (2022) 2989–3019.

[3] A. Razgordanisharahi, M. Sorgner, T. Pilgerstorfer, B. Moritz, C. Hellmich, B.L. Pichler, Realistic long-term stress levels in a deep segmented tunnel lining, from hereditary mechanics-informed evaluation of strain measurements, Tunneling Undergr. Space Technol. 145 (2024) 105602.

[4] Z.P. Bazant, M.H. Hubler, Q. Yu, Pervasiveness of excessive segmental bridge deflections: Wake-up call for creep, ACI Struct. J. 108 (6) (2011) 766.

[5] S. Li, Y. Yang, Q. Pu, D. Yang, B. Sun, X. Li, Three-dimensional nonlinear creep and shrinkage effects of a long-span prestressed concrete box girder bridge, Struct. Concr. 20 (2) (2019) 638–649.

[6] F. Benboudjema, J.-M. Torrenti, Early-age behaviour of concrete nuclear containments, Nucl. Eng. Des. 238 (10) (2008) 2495–2506.

[7] M. Briffaut, F. Benboudjema, J.M. Torrenti, G. Nahas, Numerical analysis of the thermal active restrained shrinkage ring test to study the early age behavior of massive concrete structures, Eng. Struct. 33 (4) (2011) 1390–1401.

[8] D.-M. Bouhjiti, J. Baroth, F. Dufour, S. Michel-Ponnelle, B. Masson, Stochastic finite elements analysis of large concrete structures' serviceability under thermo-hydro-mechanical loads–Case of nuclear containment buildings, Nucl. Eng. Des. 370 (2020) 110800.

[9] Z.P. Bažant, S.-S. Kim, Nonlinear creep of concrete - Adaptation and flow, ASCE J. Eng. Mech. Div. 105 (3) (1979) 429–446.

[10] M.F. Ruiz, A. Muttoni, P.G. Gambarova, Relationship between nonlinear creep and cracking of concrete under uniaxial compression, J. Adv. Concr. Technol. 5 (3) (2007) 383–393.

[11] Z.P. Bažant, A.B. Hauggaard, S. Baweja, F.-J. Ulm, Microprestress-solidification theory for concrete creep. I: Aging and drying effects, J. Eng. Mech. 123 (11) (1997) 1188–1194.

[12] Z.P. Bažant, M. Jirásek, Creep and Hygrothermal Effects in Concrete Structures, vol. 225, Springer, 2018.

[13] C. Mazzotti, M. Savoia, Nonlinear creep damage model for concrete under uniaxial compression, J. Eng. Mech. 129 (9) (2003) 1065–1075.

[14] P. Havlásek, M. Jirásek, Multiscale modeling of drying shrinkage and creep of concrete, Cem. Concr. Res. 85 (2016) 55–74.

[15] A. Sellier, S. Multon, L. Buffo-Lacarrière, T. Vidal, X. Bourbon, G. Camps, Concrete creep modelling for structural applications: non-linearity, multi-axiality, hydration, temperature and drying effects, Cem. Concr. Res. 79 (2016) 301–315.

[16] N. Reviron, F. Benboudjema, J. Torrenti, G. Nahas, A. Millard, Coupling between creep and cracking in tension, in: 6th International Conference on Fracture Mechanics of Concrete and Concrete Structures, Catania, 2007, pp. 495–502.

[17] J. Torrenti, V. Nguyen, H. Colina, F. Le Maou, F. Benboudjema, F. Deleruyelle, Coupling between leaching and creep of concrete, Cem. Concr. Res. 38 (6) (2008) 816–821.

[18] P. Rossi, J.-L. Tailhan, F. Le Maou, L. Gaillet, E. Martin, Basic creep behavior of concretes investigation of the physical mechanisms by using acoustic emission, Cem. Concr. Res. 42 (1) (2012) 61–73.

[19] J. Saliba, A. Loukili, F. Grondin, J.-P. Regoin, Identification of damage mechanisms in concrete under high level creep by the acoustic emission technique, Mater. Struct. 47 (6) (2014) 1041–1053.

[20] S.I. Diaz, H.K. Hilsdorf, Fracture Mechanisms of Concrete Under Static, Sustained, and Repeated Compressive Loads, Tech. Rep., University of Illinois Engineering Experiment Station, 1971.

[21] S.D. Santiago, H.K. Hilsdorf, Fracture mechanisms of concrete under compressive loads, Cem. Concr. Res. 3 (4) (1973) 363–388.

[22] H. Rüsch, Researches toward a general flexural theory for structural concrete, J. Am. Concr. Inst. 57 (1) (1960) 1–28.

[23] I. Fischer, B. Pichler, E. Lach, C. Terner, E. Barraud, F. Britz, Compressive strength of cement paste as a function of loading rate: Experiments and engineering mechanics analysis, Cem. Concr. Res. 58 (2014) 186–200.

[24] D. Tasevski, M.F. Ruiz, A. Muttoni, Compressive strength and deformation capacity of concrete under sustained loading and low stress rates, J. Adv. Concr. Technol. 16 (8) (2018) 396–415.

[25] A. Sousa Coutinho, A contribution to the mechanism of concrete creep, Mater. Constr. 10 (1977) 3–16.

[26] C. Mazzotti, M. Savoia, Nonlinear creep, Poisson's ratio, and creep-damage interaction of concrete in compression, Mater. J. 99 (5) (2002) 450–457.

[27] Z. Kammouna, M. Briffaut, Y. Malecot, et al., Experimental study of the creep effect on the mechanical properties of concrete, Adv. Civ. Eng. 2019 (2019).

[28] Z. Kammouna, M. Briffaut, Y. Malecot, Mesoscopic simulations of concrete strains incompatibilities under high creep stress level and consequences on the mechanical properties, Eur. J. Environ. Civ. Eng. 23 (7) (2019) 879–893.

[29] A. Tsitova, F. Bernachy-Barbe, B. Bary, F. Hild, Experimental and numerical analyses of the interaction of creep with mesoscale damage in cementitious materials, Mech. Mater. (2023) 104715.

[30] Z.P. Bažant, S. Prasannan, Solidification theory for concrete creep. II: Verification and application, J. Eng. Mech. 115 (8) (1989) 1704–1725.

[31] S. Scheiner, C. Hellmich, Continuum microviscoelasticity model for aging basic creep of early-age concrete, J. Eng. Mech. 135 (4) (2009) 307–323.

[32] G. Pickett, The effect of change in moisture-content on the crepe of concrete under a sustained load, in: Journal Proceedings, Vol. 38, 1942, pp. 333–356.

[33] P. Acker, F.-J. Ulm, Creep and shrinkage of concrete: physical origins and practical measurements, Nucl. Eng. Des. 203 (2–3) (2001) 143–158.

[34] P. Suwanmaneechot, A. Aili, I. Maruyama, Creep behavior of CSH under different drying relative humidities: Interpretation of microindentation tests and sorption measurements by multi-scale analysis, Cem. Concr. Res. 132 (2020) 106036.

[35] Y. Anderberg, S. Thelandersson, Stress and Deformation Characteristics of Concrete at High Temperatures: Experimental Investigation and Material Behaviour Model, Lund Institute of Technology Lund, Sweden, 1976.

[36] E. Binder, M. Königsberger, R. Díaz Flores, H.A. Mang, C. Hellmich, B.L. Pichler, Thermally activated viscoelasticity of cement paste: Minute-long creep tests and micromechanical link to molecular properties, Cem. Concr. Res. 163 (2023) 107014.

[37] M. Shahidi, B. Pichler, C. Hellmich, Viscous interfaces as source for material creep: a continuum micromechanics approach, Eur. J. Mech. A Solids 45 (2014) 41–58.
[38] M. Shahidi, B. Pichler, R. Wendner, S. Scheiner, C. Hellmich, Interfacial micromechanics assessment of rheological chain models and their application to early-age creep of concrete, in: CONCREEP 10, American Society of Civil Engineers, 2015, pp. 260–269.
[39] M. Shahidi, B. Pichler, C. Hellmich, Interfacial micromechanics assessment of classical rheological models. I: Single interface size and viscosity, J. Eng. Mech. 142 (3) (2016) 04015092.
[40] M. Shahidi, B. Pichler, C. Hellmich, Interfacial micromechanics assessment of classical rheological models. II: Multiple interface sizes and viscosities, J. Eng. Mech. 142 (3) (2016) 04015093.
[41] P. Rossi, J. Tailhan, F. Le Maou, Creep strain versus residual strain of a concrete loaded under various levels of compressive stress, Cem. Concr. Res. 51 (2013) 32–37.
[42] International Federation for Structural Concrete (fib), FIB Model Code for Concrete Structures 2010, International Federation for Structural Concrete, Lausanne, Switzerland, 2013.
[43] M. Königsberger, M. Hlobil, B. Delsaute, S. Staquet, C. Hellmich, B. Pichler, Hydrate failure in ITZ governs concrete strength: A micro-to-macro validated engineering mechanics model, Cem. Concr. Res. 103 (2018) 77–94.
[44] M. Irfan-ul Hassan, M. Königsberger, R. Reihsner, C. Hellmich, B. Pichler, How water-aggregate interactions affect concrete creep: Multiscale analysis, J. Nanomechanics Micromechanics 7 (4) (2017) 04017019.
[45] Z. Jiang, Z. Sun, P. Wang, Autogenous relative humidity change and autogenous shrinkage of high-performance cement pastes, Cem. Concr. Res. 35 (8) (2005) 1539–1545.
[46] M.-P. Yssorche-Cubaynes, J. Ollivier, La microfissuration d'autodessiccation et la durabilité des BHP et BTHP, Mater. Struct. 32 (1) (1999) 14.
[47] P. Rossi, N. Godart, J. Robert, J. Gervais, D. Bruhat, Investigation of the basic creep of concrete by acoustic emission, Mater. Struct. 27 (1994) 510–514.
[48] K. Ohno, M. Ohtsu, Crack classification in concrete based on acoustic emission, Constr. Build. Mater. 24 (12) (2010) 2339–2346.
[49] A. Carpinteri, G. Lacidogna, M. Corrado, E. Di Battista, Cracking and crackling in concrete-like materials: A dynamic energy balance, Eng. Fract. Mech. 155 (2016) 130–144.
[50] J. Desrues, P. Bésuelle, H. Lewis, Strain localization in geomaterials, Geol. Soc. Lond. Spec. Publ. 289 (1) (2007) 47–73.
[51] A. Simone, G.N. Wells, L.J. Sluys, From continuous to discontinuous failure in a gradient-enhanced continuum damage model, Comput. Methods Appl. Mech. Engrg. 192 (41–42) (2003) 4581–4607.
[52] L. Boltzmann, Zur Theorie der elastischen Nachwirkungen. [In German] (Concerning the theory of the elastic aftereffect), Sitz.ber. Akad. Mathematisch-Naturwissenschaftlichen Cl. Kais. Akad. Wiss. 70 (2) (1874) 275–306.
[53] M.E. Gurtin, E. Sternberg, On the linear theory of viscoelasticity, Arch. Ration. Mech. Anal. 11 (1) (1962) 291–356.
[54] A. Zaoui, Continuum micromechanics: survey, J. Eng. Mech. 128 (8) (2002) 808–816.
[55] L. Dormieux, D. Kondo, F.-J. Ulm, Microporomechanics, John Wiley & Sons, 2006.
[56] B. Pichler, C. Hellmich, H. A. Mang, A combined fracture-micromechanics model for tensile strain-softening in brittle materials, based on propagation of interacting microcracks, Int. J. Numer. Anal. Methods Geomech. 31 (2) (2007) 111–132.
[57] T. Mori, K. Tanaka, Average stress in matrix and average elastic energy of materials with misfitting inclusions, Acta Metall. 21 (5) (1973) 571–574.
[58] Y. Benveniste, A new approach to the application of Mori-Tanaka's theory in composite materials, Mech. Mater. 6 (2) (1987) 147–157.
[59] L. Dormieux, D. Kondo, Poroelasticity and damage theory for saturated cracked media, in: Applied Micromechanics of Porous Materials, Springer, 2005, pp. 153–186.
[60] N. Laws, R. McLaughlin, Self-consistent estimates for the viscoelastic creep compliances of composite materials, Proc. R. Soc. A 359 (1697) (1978) 251–273.
[61] B. Budiansky, R.J. O'Connell, Elastic moduli of a cracked solid, Int. J. Solids Struct. 12 (2) (1976) 81–97.
[62] B. Pichler, L. Dormieux, Potentials and limitations of Griffith's energy release rate criterion for mode I type microcracking in brittle materials, Bifurcations, Instab. Degrad. Geomech. (2007) 245–276.
[63] M. Königsberger, M. Irfan-ul Hassan, B. Pichler, C. Hellmich, Downscaling based identification of nonaging power-law creep of cement hydrates, J. Eng. Mech. 142 (12) (2016) 04016106.
[64] J. Glucklich, O. Ishai, Creep mechanism in cement mortar, ACI J. Proc. 59 (7) (1962) 923–948.
[65] W. Mullen, W. Dolch, Creep of Portland cement paste, in: Proceedings of the American Society of Testing Materials, Vol. 64, 1964, pp. 1146–1171.
[66] N.H. Brown, B.B. Hope, The creep of hydrated cement paste, Cem. Concr. Res. 6 (4) (1976) 475–485.
[67] A. Neville, The measurement of creep of mortar under fully controlled conditions, Mag. Concr. Res. 9 (25) (1957) 9–12.
[68] F. Wittmann, Interaction of hardened cement paste and water, J. Am. Ceram. Soc. 56 (8) (1973) 409–415.
[69] S. Granger, A. Loukili, G. Pijaudier-Cabot, G. Chanvillard, Experimental characterization of the self-healing of cracks in an ultra high performance cementitious material: Mechanical tests and acoustic emission analysis, Cem. Concr. Res. 37 (4) (2007) 519–527.
[70] M. Omar, A. Loukili, G. Pijaudier-Cabot, Y. Le Pape, Creep-damage coupled effects: experimental investigation on bending beams with various sizes, J. Mater. Civ. Eng. 21 (2) (2009) 65–72.
[71] J. Saliba, A. Loukili, J.-P. Regoin, D. Grégoire, L. Verdon, G. Pijaudier-Cabot, Experimental analysis of crack evolution in concrete by the acoustic emission technique, Frat. Ed Integrità Strutt. 9 (34) (2015).
[72] G. Pijaudier-Cabot, Z.P. Bažant, Nonlocal damage theory, J. Eng. Mech. 113 (10) (1987) 1512–1533.
[73] A. Delaplace, G. Pijaudier-Cabot, S. Roux, Progressive damage in discrete models and consequences on continuum modelling, J. Mech. Phys. Solids 44 (1) (1996) 99–136.
[74] G. Pijaudier-Cabot, Fracture and permeability of concrete and rocks [Rupture et perméabilité des bétons et des roches], C. R. Phys. 21 (6) (2020) 507–525.
[75] M. Ausweger, E. Binder, O. Lahayne, R. Reihsner, G. Maier, M. Peyerl, B. Pichler, Early-age evolution of strength, stiffness, and non-aging creep of concretes: Experimental characterization and correlation analysis, Materials 12 (2) (2019) 207.